TECHNISCHE UNIVERSITÄT WIEN
Vienna | Austria

Dr. techn. Andreas LIMBECK

VIENNA UNIVERSITY OF TECHNOLOGY

DIPLOMARBEIT

Insights into the PLD Process via ICP-MS Analysis of LSCF Model-Type Thin Films

Author:

Christopher HERZIG B.Sc.

Supervisor:

Associate Prof. Dipl.-Ing.
Dr. techn. Andreas LIMBECK
Univ.Ass. Dipl.-Ing. Dr. techn.
Alexander Karl OPITZ

A thesis submitted in fulfillment of the requirements
for the degree of Master of Science
at the
Institute of Chemical Technologies and Analytics

Christopher HERZIG, B.Sc.
Mühlplatz 4, 3484 Grafenwörth

November 2017, Vienna

Abstract

Alternative forms of energy storage and conversion are gaining more and more importance in the 21^{st} century, especially with regard to environmental and efficiency problems of combustion engines used today. Solid oxide fuel cells (SOFC) are electrochemical devices providing the conversion of chemical energy in fuels (e.g. H_2, methane or other liquid energy sources) into electricity with a very high conversion efficiency. To meet the requirements, the development of new electrode materials with high catalytic activity for oxygen reduction and other tailored characteristics are necessary. To further improve the efficiency of today's SOFCs and thus making them also economically more competitive, a reduction of their operation temperature is aimed at. Among others, lanthanum strontium cobalt ferrite (LSCF) offers high activity for oxygen reduction and is already successfully used as cathode material in SOFCs. The performance as well as the degradation behaviour of these materials, however, is strongly dependent on their stoichiometry. Therefore, accurate measurement of the elemental composition is absolutely necessary for a knowledge-based improvement of LSCF and related cathode materials.

In this work, the production and analysis of LSCF thin films is investigated. The thin films were produced with a technique called pulsed laser deposition (PLD). Thereby the material is ablated from a target using an UV-laser and deposited as a dense thin film on the substrate. The obtained thin films were used as model system to investigate the elemental composition and learn about the Sr segregation at SOFC operation conditions.

As an analytical method for Sr quantification, inductively coupled plasma-mass spectrometry (ICP-MS) was used. From previous work it is known that at temperatures above 500 °C Sr segregates to the surface of the thin films and forms water soluble Sr species. The aqueous solutions needed for ICP-MS measurements were obtained via two different steps. The first one is a H_2O etching and the second one a HCl etching method. In the first step, only water soluble species are dissolved. The amount of water soluble Sr species can be determined in this kind of experiments. In the second step, the remaining LSCF film was completely dissolved with HCl and the stoichiometry of the deposited film could be calculated from the corresponding ICP-MS results.

These liquid ICP-MS measurements gave hints that the lateral distribution of cations in the deposited thin films on 4 samples per PLD run are not homogeneous. This finding was the starting point to a more detailed investigation of the PLD process.

Therefore, PLD parameters were varied and a significant improvement in the homogeneity of the thin films could be achieved. Increasing the substrate to target distance turned out to be a crucial factor for film stoichiometry. The lateral distribution of cations within the film was characterised with a laser ablation (LA) system connected to the ICP-MS equipment. By this technique it was possible to analyse a solid sample without the need of dissolving the sample and thereby losing spatial information. Lateral elemental variations of a sample of 4.5 cm in diameter could be mapped in a single measurement run. By using an appropriate software, images of the elemental distribution of films deposited with PLD could be obtained. Such elemental distribution images are a unique feature of the used techniques and are a large step forward in understanding the dynamics and elemental distribution within the plasma plume in the PLD process.

Having improved the homogeneity of the samples of one PLD run, several annealing experiments were executed to study the segregation behaviour of Sr under conditions similar to those in an operating SOFC. The samples were annealed in dry and humidified synthetic air at 800 °C for different periods of time. From this experimental setup, time depending information about the segregation could be obtained. Furthermore it could be seen that the amount of humidity in the gas stream is of great importance in the formation process of water soluble Sr species. In a dry atmosphere about 3.5 monolayers of SrO are formed at the surface of the sample. Only 2.5 monolayers of SrO are formed in a dry atmosphere, but the formation process under this conditions is four times faster than in under humid conditions. This information is important for our co-workers in the Christian Doppler Laboratory in which framework this work was conducted.

Kurzfassung

Alternative Formen der Energiegewinnung stehen im Blickpunkt der Forschung zu Beginn des 21. Jahrhunderts. Die Fragen des Umweltschutzes und die Tatsache der endlichen fossilen Energieträger lässt die Suche nach effizienteren und umweltfreundlicheren Technologien an Bedeutung gewinnen. Festoxidbrennstoffzellen (Englisch *solid oxide fuel cell*, SOFC) bieten die Möglichkeit chemische Energie, die in Form von Wasserstoff, Methanol oder anderen flüssigen Energieträgern gespeichert ist, in elektrische Energie mit hoher Effizienz und sehr geringem Schadstoffausstoß umzuwandeln. Für diese Technologie sind allerdings Materialien mit besonderen Stoffeigenschaften nötig. Lanthanstrontiumcobalteisenoxid (LSCF) ist ein Vertreter dieser Substanzen, die als Kathodenmaterial in Brennstoffzellen Anwendung finden können. Da die Materialeigenschaften stark von ihrer Stöchiometrie abhängen, ist eine akkurate Bestimmung der Elementzusammensetzung notwendig.

In der hier vorliegenden Arbeit wurden LSCF Dünnfilme mittels Laserdeposition (Englisch *pulsed laser deposition*, PLD) hergestellt und mittels Massenspektrometrie mit induktiv gekoppeltem Plasma (ICP-MS) vermessen. Beim PLD-Prozess wird das Target mit einem gepulsten UV-Laser bestrahlt, wodurch Material abgetragen und ionisiert wird. Auf dem beheizten Substrat scheidet sich LSCF unter passenden Bedingungen als kompakte Dünnschicht wieder ab.

Wie bereits in der Literatur vielfach gezeigt werden konnte, segregiert Sr an die Oberfläche eines LSCF Films und bildet dort wasserlösliche Sr-Spezies aus. Die quantitative Bestimmung dieses Sr erfolgte mittels ICP-MS. Dazu wurden die Proben für eine gewisse Zeit in Wasser getaucht und die so erhaltene Lösung vermessen. Für eine quantitative Bestimmung der Zusammensetzung des LSCF Films wurde die Probe mit konzentrierter Salzsäure vollständig aufgelöst. Aufgrund der Quantifizierung mittels Flüssigstandards konnte aus den gemessenen Verhältnissen die Stöchiometrie der abgeschiedenen LSCF Schicht bestimmt werden.

Wie sich bereits in den Ergebnissen der ICP-MS Flüssigmessungen zeigte, weisen die vier Proben, die pro Abscheidung hergestellt werden können, deutliche Unterschiede in ihrer chemischen Zusammensetzung auf. Diese Erkenntnis war der Ausgangspunkt, den Abscheideprozess zu untersuchen und zu optimieren. Durch die Vergrößerung des Abstandes zwischen Target und Substrat konnte eine signifikante Verbesserung der Homogenität der vier Proben eines PLD-Prozesses erzielt werden.

Mithilfe eines Laser Ablationssystems (LA), das mit dem Massenspektrometer verbunden ist, war es möglich, eine feste Probe örtlich aufgelöst zu vermessen. Dazu wurde eine Aluminiumoxidscheibe mit 4,5 cm Durchmesser mit LSCF beschichtet und mit dem Laser Punkt für Punkt abgerastert. Mit einer entsprechenden Software ist es möglich, die Elementverhältnisse, die in jedem Punkt gemessen wurden, graphisch darzustellen. Als Resultat erhält man Elementverteilungsbilder (sogenannte *images*), die deutlich die laterale Inhomogenität des Abscheideprozesses sichtbar machen. Solche images von Dünnschichten, die mittels PLD-Prozess hergestellt wurden, konnte in der Literatur nicht gefunden werden.

Mit den optimierten Abscheidebedingungen wurden Proben hergestellt, deren Sr Segregationsverhalten bei Betriebsbedingungen untersucht wurde. Dazu wurden die Proben in trockener oder angefeuchteter synthetischer Luft unterschiedlich lange bei 800 °C ausgelagert. Anschließend wurde die Menge an wasserlöslichem Sr mittels ICP-MS bestimmt. Die Ergebnisse zeigen, dass der Feuchtigkeitsgehalt in der Atmosphäre einen großen Einfluss sowohl auf die Geschwindigkeit der $SrO/Sr(OH)_2$ Bildung, als auch auf die Menge der gebildeten wasserlöslichen Sr-Spezies hat. In trockener Atmosphäre werden 3.5 Monolagen SrO an der Oberfläche der Proben gebildet. Wird die Atmosphäre befeuchtet, so reduziert sich die Menge an Sr an der Oberfläche auf 2.5 Monolagen SrO. Die SrO Bildungsgeschwindigkeit ist unter feuchten Bedingungen 4-mal schneller, als unter trockenen Bedingungen. Diese Daten sind wichtige Informationen für die Projektpartner des Christian Doppler Labors, in dessen Rahmen auch diese Diplomarbeit durchgeführt wurde.

Danksagung

Diese akademische Arbeit bildet in gewisser Hinsicht den Schlussstein eines mehr oder weniger großen Gewölbes meiner bisherigen schulischen und unversitären Laufbahn. Sie ist als ein kleiner, aber wie der Schlussstein, sehr wichtiger Teil zu verstehen. Daher bietet sich nun eine wunderbare Gelegenheit, den vielen Menschen, die direkt oder indirekt zum Gelingen dieses Vorhabens beigetragen haben, zu danken.

Auf den letzten Metern direkt dazu beigetragen haben Andreas Limbeck, Alexander Opitz, Maximilian Bonta und Matthias Gerstl. Den beiden Erstgenannten ist dafür zu danken, dass sie mir die Möglichkeit zur Durchführung dieser Arbeit in ihren Forschungsgruppen gegeben haben. Die intensive Zusammenarbeit der beiden Forschungsbereiche war für mich auf jeden Fall eine Bereicherung. Ich hoffe, dass diese Verbindung noch weitere fruchtbringende Zeiten erlebt.

Maximilian Bonta und Matthias Gerstl haben mit ihren praktischen Erfahrungen im Bereich der Analytik und der Elektrochemie viel zum Gelingen der Arbeit beigetragen. Danke, dass ihr mir so viel Zeit gewidmet und euer Wissen mit mir geteilt habt.

Um erst in die Verlegenheit zu kommen, eine Diplomarbeit zu schreiben, muss auch das Studium Fortschritte machen. Diese Fortschritte wären ohne meine Studienkollegen nicht so rasch möglich gewesen. Besonders mit Stefan Leopold-Messer, Lukas Brunnbauer, Anna Haydn, Dorian Bader, Barbara Dellago, Martin Jäger und Elke Ludwig verbinden mich viele intensive Stunden des Lernens, des Arbeitens im Labor, des Feierns, der Musik und der politischen Diskussion. Ich danke euch für eure Gesellschaft, wodurch die Studienzeit zu einer sehr schönen Erfahrung wurde.

Abseits des Studiums haben mir besonders meine ehemaligen Schulkollegen und Freunde Andreas Steininger, Tobias Riedl, Agnes Mantler und Selma Kaya stets den Horizont erweitert und mich durch persönlich schwierige Zeiten begleitet. Danke dafür, dass wir immer noch gemeinsame Interessen teilen. All jenen, die ich nicht namentlich nennen konnte und die trotzdem vieles mit mir verbindet, sei verischert, dass ich ihnen dankbar für ihre Gesellschaft bin.

Das Fundament, um die anfängliche Metaphorik wieder aufzugreifen, für diese schöne Zeit und den Luxus eines Studiums hat meine Familie gelegt. Für die Ermöglichung einer solchen schulischen und akademischen Laufbahn gebührt meiner Mutter und meinem Vater († 2015) besonderer Dank.

Contents

List of Abbreviations

AFM	atomic force microscopy
EDS	energy dispersive spectroscopy
FC	fuel cell
GDC	gadolinium doped cerium oxide
ICP-MS	inductively coupled plasma-mass spectrometry
ICP-OES	inductively coupled plasma-optical emission spectroscopy
LA-ICP-MS	laser ablation-inductively coupled plasma-mass spectrometry
LEIS	low energy ion scattering
LOD	limit of detection
LSC	lanthanum stronium cobaltite
LSCF	lanthanum strontium cobalt ferrite
MBE	molecular beam epitaxy
MIEC	mixed ionic and electronic conductor
ORR	oxygen reduction reaction
PAD	polymer assisted deposition
PLD	pulsed laser deposition
RBS	Rutherford backscattering spectroscopy
RSD	relative standard deviation
SEM	scanning electron microscopy
SOFC	solid oxide fuel cell
TEC	thermal extension coefficient
XPS	x-ray photoemission spectroscopy
YSZ	yttrium stabilised zirconium dioxide

Chapter 1

Introduction

Electricity is considered to be the most convenient form of energy, because it is low in emission and very flexible at the point of use compared to fossil fuels, which are converted for example in a combustion engine. Therefore, it is expected that the world net electricity generation will double in the years from 2010 to 2040 [1]. Because of environmental and/or economic issues the way of converting primary energy carriers into electrical power is critical. From the 19^{th} century on, combustion engines, starting with the steam engine, have been widely used for transforming the chemical energy stored in fossil fuels into thermal, kinetic or electrical energy. One drawback of these devices is the low conversion efficiency due to several steps being necessary for the conversion of chemical energy into electrical energy. Nowadays, combined cycle plants with sophisticated and very expensive opimization reach thermal efficiency values of about 58 % [2]. In contrary, fuel cells (FC) offer an alternative conversion route from chemical to electrical energy without any intermediate steps. Hence, efficiency values exceeding 70 % for FCs are possible. These electrochemical devices could meet the high standards concerning environmental and ecological aspects of energy supply for societies in the 21^{st} century.

Solide oxide fuel cells (SOFCs) working in the intermediate temperature range (700-500 °C) are promising candidates within the wide variety of possible FC designs. The materials used in this kind of FCs have to exhibit special characteristics. As electrolyte an ion conducting ceramic (such as Yttrium-stabilised Zirconiumdioxide, YSZ) is used. The elevated temperatures are needed to provide a sufficiently high ionic conductivity. As cathode materials, so called mixed ionic and electronic conductors (MIEC), perovskite-type oxides are of great interest [3]. These materials exhibit the ability of conducting electrons as well as oxygen ions under working conditions. $La_{1-x}Sr_xCoO_{3-\delta}$ (LSC) was the first material of this kind reported in 1966, showing fairly high ionic and electronic conductivity. Another very well investigated MIEC is $La_{1-x}Sr_xMnO_{3-\delta}$ (LSM) [4] with much higher stability but lower conductivity in contrary. But conductivity of the electrode is not solely a warrantor for an optimal operating SOFC. Additional parameters like thermal expansion coefficients (TEC), reaction kinetics, manufacturing processes, intended purpose (mobile or stationary use), and many more have to be considered for the construction of

SOFCs. The presented work will deal with $La_{0.58}Sr_{0.40}Co_{0.20}Fe_{0.80}O_{3-\delta}$ (LSCF), because it shows a high activity for the oxygen reduction reaction (ORR) at the desired SOFC operation temperatures and is in the focus of ongoing research. Providing reliable analytical methods for these kind of materials is of great interest for the research community.

Previous work has shown that there is a substantial degradation behaviour of LSCF as a cathode material. Simner et al. [5] report degradation rates of 0.26 % per hour in the first 50 hours of operation and 0.0047 % per hour afterwards. Furthermore, many evidence could be found for Sr surface enrichment during the degradation process [6–11]. Cai et. al. discussed the presence of $SrO/Sr(OH)_2$with X-ray photo-electron spectroscopy and Auger electron spectroscopy for LSF thin films and Kubicek et. al [6] could show the presence of SrO/ $Sr(OH)_2$ on the surface of LSC thin films with inductively coupled plasma-optical emission spectroscopy (ICP-OES) by etching with diluted hydrochloric acid. Limbeck et al. [12] made steps to further develop an ICP-MS method for quantifying the Sr-rich surface layer. The idea behind is, that $Sr(OH)_2$ is sufficiently soluble in H_2O whereas the solubility of the LSCF-perovskite in neutral H_2O is negligible. Lowering the pH-value leads to an increased solubility of the LSCF-perovskite. This very subtle selective etching technique is used in this work, too. The resulting etching solutions are ideal samples for liquid ICP-MS measurements, because of the possibility of quantification by liquid standard solutions.

Applying and evaluating the above described etching method on LSCF thin films produced by pulsed laser deposition (PLD) is the main task of the presented work. Furthermore, determining the elemental composition of the whole perovskite film was required. Therefore, liquid ICP-MS was used, because it is a powerful and reliable tool for multi-element analysis with very low detection limits. The content of the elements analysed in the samples obtained by the H_2O etching procedure were in the low µg/L range or even lower. With the available ICP-MS equipment it was possible to analyse these low concentrations satisfyingly.

The synthesis of the thin films was done by PLD in house. Experiments at the beginning showed substantial relative standard deviations (RSD) of the measured Sr value of the H_2O etching solutions. Even the RSD values of four samples produced in one run ranged between 9 and 18 %. The overall RSD value of 16 samples produced and measured consecutively was as high as 15 %, which is still substantial and should be investigated. As a consequence, small changes of the Sr content in subsequent experiments could be covered by this unsatisfactory deviation and thus not be detected. By varying the parameters of the PLD process the RSD values of the water soluble Sr amount could be significantly reduced. Beyond the investigated parameters the distance between the substrate, where the thin film should be

deposited and the target, was the one with most influence. An optimal value, with respect to the Sr value in the H_2O etching process, could be found.

With the new set of PLD-parameters, it was possible to produce samples which usually exhibited approximately 3 % RSD. Because of this low RSD value, small changes in the Sr amount on the surface can be detected. Making use of the better measurement quality, several annealing experiments were executed to enhance the Sr segregation. In these experiments, dry or humidified synthetic air was used. The samples were annealed at 800 °C for different periods of time. The presence or absence of H_2O caused a significant difference in the Sr segregation behaviour.

The experiments with the common PLD-parameters indicated inhomogeneities between the four samples of one batch. For a more detailed investigation a bigger sample with a diameter of 4.5 cm was produced and probed with laser ablation-inductively coupled plasma-mass spectrometry (LA-ICP-MS) to obtain spatially resolved information. The resulting data indeed showed that there is elemental variation over the sample area. With this experiment it could be confirmed that the poor data quality at the beginning of the experiments was not due to problems of the actual measurement, but due to the thin film preparation process. It has to be mentioned that the data derived form LA-ICP-MS could only be interpreted in terms of relative differences, because no calibration standard was available.

Chapter 2

Theoretical Aspects

2.1 Fuel Cell

Fuel cells (FC) are electrochemical devices which convert the chemical energy of fuel into electrical and thermal energy. Like every electrochemical cell, FCs consist of an anode, cathode, electrolyte and an external circuit for the electron current. The difference between batteries - which are the more common electrochemical cells in everday life - and FCs is that FCs can be operated continuously while batteries have to be charged from time to time. FCs can roughly be described as continuously operating batteries. Two half-cell reactions (oxidation of the fuel at the anode and reduction of the oxygen at the cathode) happen separated from each other by an electrolyte. The electrolyte is only conductive for ions and insulating for electrons. The electrons have to run the external circuit. An illustration for SOFCs is given in figure 2.1. FCs offer major advantages like high efficiency, because of the direct conversion of the fuel into heat and electricity, fuel flexibility ranging from pure hydrogen to hydrocarbons (only with SOFC possible), and minimization of emitted pollutants as SO_2 or NO_x. Furthermore FCs can be easily scaled up: from portable electricity supplier to the size of power plants, every dimension is possible. FCs are denoted as environmentally friendly and could replace the classical combustion engines, because protecting the environment and handling the issue of finite fossil fuels are important topics at the beginning of the 21^{st} century. Although huge scientific effort has been made and some milestones have been reached in the last few decades, FCs have not reached the middle of society yet. The significantly high costs of production prevent a fast commercialisation. [4]

Within the time a wide variety of FCs regarding the materials used as electrodes and electrolyte, the operating temperature, the kind of fuel which can be used, and the stack design (planar or tubular) has developed. The investigated material in this work can be used for SOFCs. Therefore more details on this type in FCs is presented in the next sections.

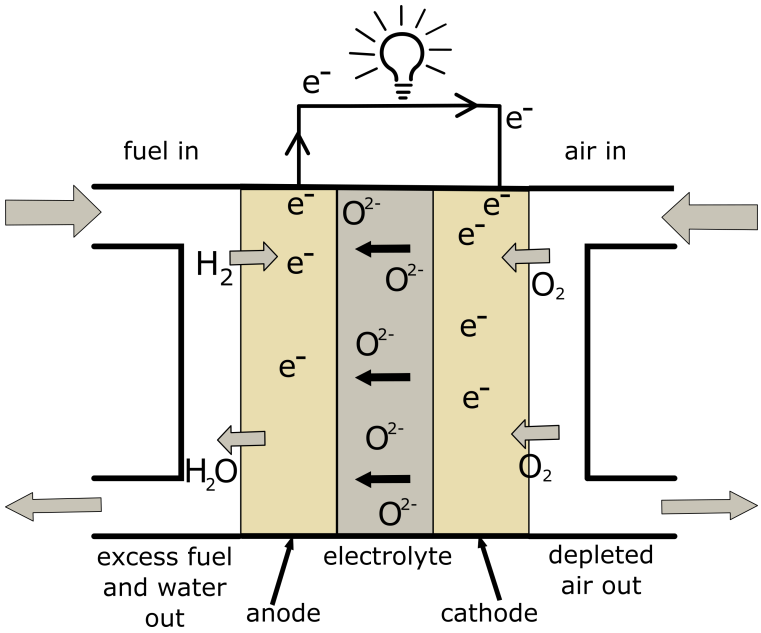

FIGURE 2.1: Schematic diagram of a SOFC with oxide-ion conducting electrolyte; H_2 as fuel is oxidised by O_2; separating the oxidation and reduction reaction by an electrolyte leads to an external electron current;

2.1.1 Solide Oxide Fuel Cell (SOFC)

The main discriminating element of SOFCs from other FC-types is the solid electrolyte, which is capable of conducting oxygen ions. This kind of material was initially discovered by Gaugin in 1853. Many famous scientists like Nernst, Haber, Schottky and many more have contributed to this topic already in the 19^{th} and 20^{th} century. [13]

The chemical reactions taking place at each side of the electrolyte are fairly simple, if H_2 and O_2 are used as fuel. At the cathode the O_2 molecule consumes electrons provided by the external electron current from the anode and thereby gets reduced. This can be described in following equation :

$$\mathrm{O_2 + 4\,e^- \rightleftharpoons 2\,O^{2-}} \tag{2.1}$$

After migration of the O^{2-} through the electrolyte the H_2 molecule is oxidised, emits an electron and forms water with the O^{2-} ion. This can be described as follows:

$$\mathrm{2\,O^{2-} + 2\,H_2 \rightleftharpoons 2\,H_2O + 4\,e^-} \tag{2.2}$$

The overall reaction is the well known oxyhydrogen reaction:

$$\mathrm{2\,H_2 + O_2 \longrightarrow 2\,H_2O} \tag{2.3}$$

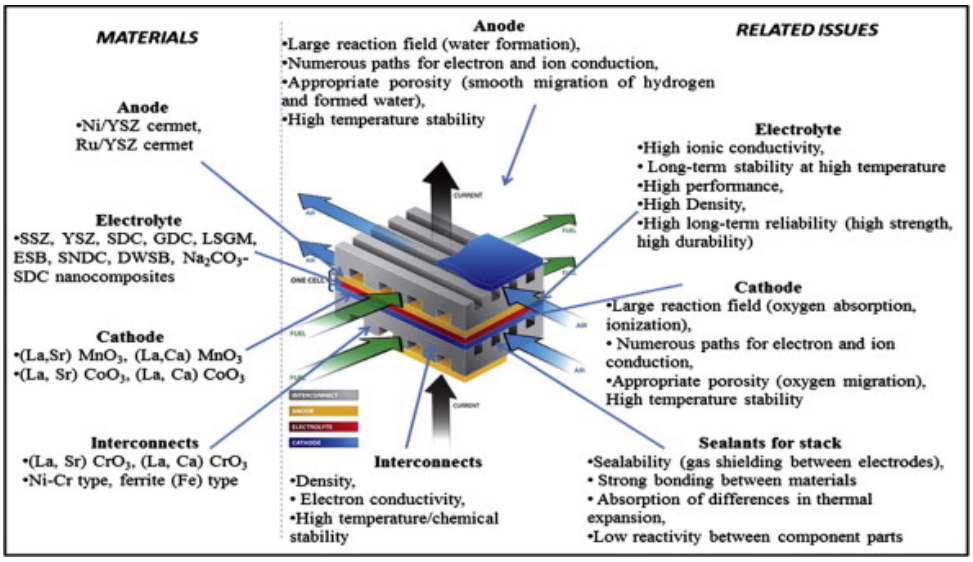

FIGURE 2.2: Summary of used materials in SOFCs and related issues [4];

Because of the use of a solid electrolyte, high operating temperatures (700-850 °C) are necessary for achieving sufficient ionic conductivity. About 0.1 S/cm is a sensible value for an electrolyte at operating temperatures. The high temperatures, however, provoke substantial further issues. The used materials in SOFCs have to withstand these temperatures as long as possible. It is also requested that they do not react with each other and that they have comparable thermal extension coefficients. Otherwise the mechanical stress during cooling down or heating up may cause failure of the stack (operative assembley of all components of a FC). Another drawback of high temperatures is, a long warm-up time and faster degradation. As one can see, there is a big interest in lowering the operating temperature of SOFCs while keeping the ionic conductivity and the kinetics of electrochemical reactions at the electrodes as high as possible. Some commonly used materials in SOFCs and their related issues are described in Figure 2.2. As anodes a composite material consisting of metallic Ni and yttrium stabilized zirconiumdioxide (Ni/YSZ cermets) is widely used. YSZ is a commonly used electrolyte. The first material used for the cathode was Pt [13] followed by the introduction of perovskite based oxides in the second half of the 20^{th} century.

2.1.2 Cathode Materials

Cathode materials have to meet certain requirements, for an efficient operation of the SOFC. Some of these are described below:

1. High electronic and ionic conductivity (materials exhibiting this behaviour are also called as mixed ionic and electronic conductor (MIEC):

   (a) The electronic conductivity should exceed 100 S/cm in an oxidising atmosphere;

   (b) The ionic conductivity should be in the same range as the electrolyte at desired operating temperatures

2. Good chemical compatibility with the electrolyte and interconnect materials:
   (a) Using YSZ and La-based cathode materials can lead to the formation of $La_2Zr_2O_7$, which reduces the performance of the FC.
   (b) Interconnects containing Cr as alloy material can cause poisoning of the cathode surface and reduce the catalytic activity for the ORR.
3. Similar thermal expansion coefficients (TEC):
   (a) Mechanical stress during heating up or cooling down may cause cell break, if TEC are too different of the used materials.
4. High catalytic reactivity for ORR
5. Sufficient porosity:
   (a) Sufficient porosity of the cathode is necessary to allow the diffusion of O_2 gas from cathode to cathode-electrolyte interface.
6. Cost effective

One kind of material meeting these requirements to a large extent are perovskite based oxides. One member of this group of materials is LSCF which is explained in more detail in the following section.

2.1.3 Perovskite Based Materials

$\mathbf{La_{0.58}Sr_{0.40}Co_{0.20}Fe_{0.80}O_{3-\delta}}$ (LSCF)

LSCF is a material which belongs to the class of perovskite based oxides. The general formula of these materials is ABO_3 (e.g., $LaMnO_3$, $LaCoO_3$, $LaFeO_3$), in which the A-sites are occupied by cations with larger ionic radii [4]. The A-sites are coordinated by twelve oxygen anions. Common A-cations are rare and alkaline earth elements, like La, Sr, Ca, Ba and usually exhibit lower valance than the B-cations. The B-sites are usually occupied by transition metal cations with smaller ionic radii and higher valences than the A-cations. Typical representatives for B-site elements are Ti, Cr, Ni, Fe, Co, Zr, etc. The B-cations are coordinated by six oxygen anions. The overall valence of the A-site and the B-site cations (n+m) adds up to 6. For both sites it is possible to have a mixture of two or more elements on the same site, which makes this class of materials very easy to modify by doping. The ideal unit cell of a perovskite has cubic closest packing and as depicted in Figure 2.3 there are two possible ways of illustrating.

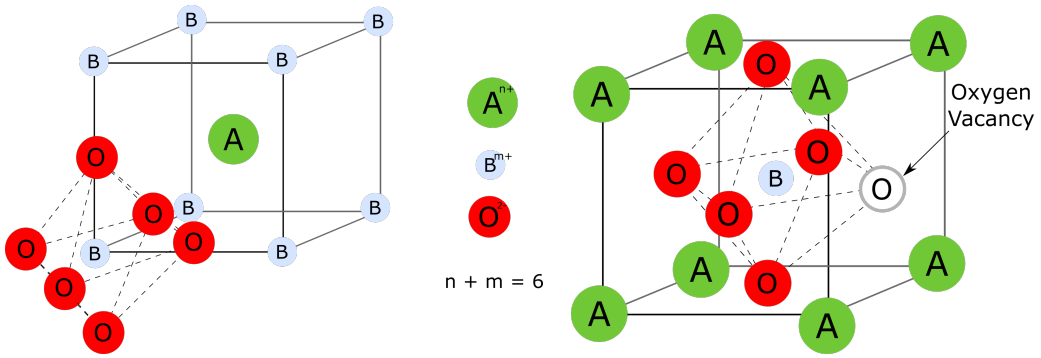

(a) A-site centred drawing of a perovskite; (b) B-site centred drawing of a perovskite;

FIGURE 2.3: Different ways of illustrating the perovskite structure;

In reality the crystal structure can be distorted due to a mismatch of the ionic radii of the used elements. With the so called Goldschmidt tolerance factor (t) it is possible to estimate the degree of distortion [14]. This factor can be calculated as follows:

$$t = \frac{r_A + r_O}{\sqrt{2}(r_B + r_O)} \tag{2.4}$$

For calculation of (t), the ionic radii of the used elements are important. Usually the Shannon's ionic radii are used for calculation, because in this figures the coordination number of each element is also taken into account. For ideal cubic structures, the tolerance factor (t) is near unity. Values smaller than one indicate orthorhombic or rhombohedral structure. For LSCF with the used stoichiometry the Goldschmidt factor is 0.71. The data for the calculation was taken from [15] (La^{3+}_{XII} = 0.136 nm, Sr^{3+}_{XII} = 0.144 nm, Co^{3+}_{VI} = 0.0578 nm and Fe^{3+}_{VI} = 0.0598 nm). For Co an Fe, where high spin and low spin configuration is possible, a 1:1 ratio was estimated. As reported in [16] LSCF with this stoichiometry has orthorhombic crystal structure.

Undoped perovskite materials are usually poor oxide ion conductors. Partially substituting the A-sites with acceptor cations like Sr^{2+}, Ca^{2+} or Ba^{2+} can result under certain conditions in the formation of oxygen vacancies. These oxygen vacancies are the basis for the oxygen conducting capability. The oxygen ions move along the edges of the octahedron by filling up oxygen vacancies with ions. Find a schematic drawing at figure 2.4 A large stable number of oxygen vacancies enhances the ionic conductivity.

The electronic conductivity characteristic of these materials can be explained by the octahedral symmetry around the transition metal. This symmetry promotes metallic or semiconducting band structures at elevated temperatures. In case of a semiconducting behaviour the electron/hole conduction can also be illustrated as a hopping mechanism via changing the oxidation state of the transition metal. See both mechanisms depicted in figure 2.4.

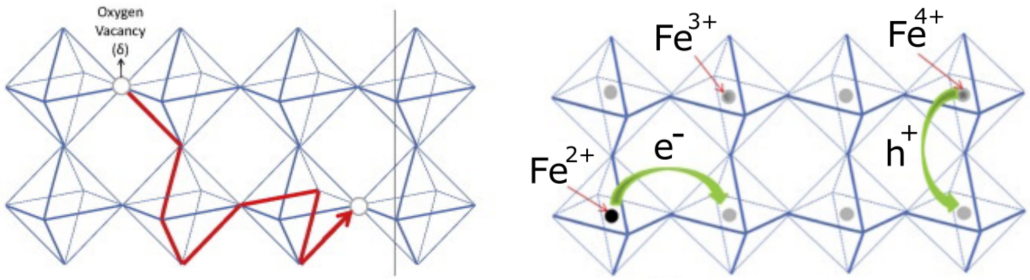

(a) Oxygen ions hop from occupied crystal sites to oxygen vacancies and thus move through the crystal;

(b) Electron/hole conduction via hopping mechanism by changing the oxidation state of the transition metal;

FIGURE 2.4: Conduction mechanisms in mixed ionic and electronic conducting oxides.[4]

2.2 Inductively Coupled Mass Spectrometry (ICP-MS)

2.2.1 Overview

ICP-MS is a versatile technique for trace element analysis. It is widely applied in many different resarch fields spanning from environmental, life and forensic sciences over chemical and material sciences to food and semiconductor industry with a still growing group of users [17]. Major advantages of this technique are very low detection limits (between 0.02 and 0.7 µg L^{-1} for most elements [18]), wide linear dynamic range (6 orders of magnitude [18]) and multi elemental detection with isotopic information [19]. Furthermore measurement times are usually quite short ranging from a few seconds to several minutes.

In general, the ICP-MS unit consists of a sample introduction system, an ICP torch for plasma generation, an interface to overcome the pressure difference between the plasma and the mass spectrometer, a vacuum system, ion lenses for focusing the ion beam, a mass analyser for separating ions with different $\frac{m}{z}$-values, an ion detector for counting the incoming ion flux and a data handling system. Some crucial parts will be described in detail in the following sections.

2.2.2 Inductively Coupled Plasma (ICP)

For inorganic mass spectrometry the inductively coupled plasma (ICP) is a widely used ionisation source. The ICP-torch usually consists of three concentric quartz tubes, which are flushed with Ar at different flow rates. At the top of the torch there is a water cooled induction coil, which is operated with alternating current (see sketch in figure 2.5). The frequency used for ICP torches is either 27.1 MHz or 40.6 MHz. This oscillation sets up strong electrical and magnetic fields. With an electrical spark it is possible to ionize some Ar atoms to Ar^+ ions. The thereby released electrons are trapped within the magnetic field applied by the induction coil and get accelerated. The electrons with high kinetic energy collide with other

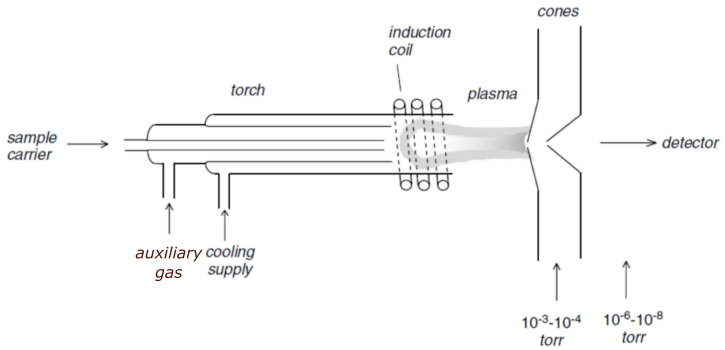

FIGURE 2.5: Schematic diagram of an ICP-torch [17] (adapted);

Ar atoms. If the velocity is high enough, the collisions can produce additional Ar^+ ions. This process (also called as inductive coupling) continues as long as enough energy is provided by the induction coil [20].

Usually these coils are operated at a power between 750 and 1700 W. The temperatures reached in the torch range between 6000 and 10 000 K, depending on the position in the plasma. This temperature is in every case high enough to evaporate the solvent (if present), vaporise the solid, break all chemical bonds (atomization) and ionize all elements, whose first ionisation energy is smaller than that of Ar (15.76 eV) [17, 20].

The three concentric quartz tubes depicted in figure 2.5 have different labels for their different purposes. The tube in the middle is carrying the sample in shape of small droplets or particles with an typical Ar flow rate of 0.5 to 1.5 L min^{-1}. The coolant gas streams in the outermost tube with flow rates between 11 and 15 L min^{-1}. The aim of this gas flow is to give the plasma a certain shape and to push the plasma away form the walls of the quartz tubing to prevent damage. The middle tube of the three delivers the auxiliary gas with typical flow rates of 0.5 to 1.5 L min^{-1}. The purpose of this stream is again preventing the inner tube from melting.

2.2.3 Sample Introduction

Within the time a wide variety of sample introduction systems have been established. Two of them shall be discussed in detail in the following, because they were used in this work.

Liquid Sample Introduction

Classically samples are introduced into ICP-MS in the form of solutions. Therefore the liquid has to be nebulized. This is usually done by a so called Meinhard-nebulizer which consists of two concentric tubes. The inner one contains the liquid

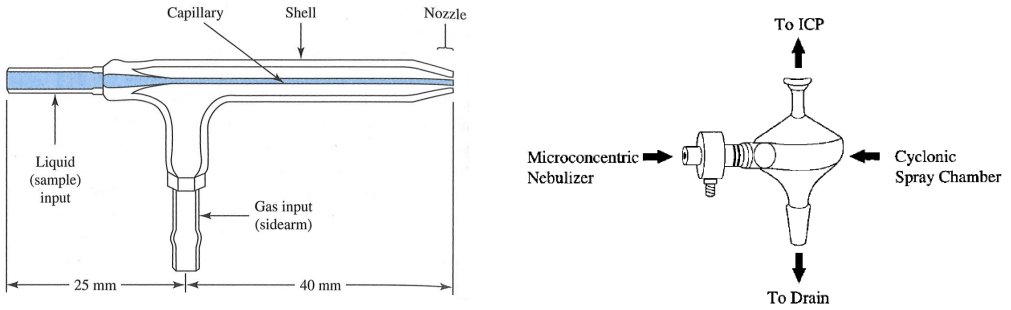

(a) Meinhard nebulizer consisting of two concentric tubes, one is for the liquid, the other one is for the gas flow for nebulization; [18]

(b) Cyclonic spray chamber for elimination of big droplets of the aerosol;[21]

FIGURE 2.6: Elements for liquid sample introduction;

and the outer one provides an Ar stream, which produces a suction effect at the nozzle and aspirates the sample. Due to the high flow velocity at the narrow nozzle the liquid is sprayed and many droplets are produced (see figure 2.6 a)). The aim is to produce as many small droplets as possible. The Ar stream is directed in a way that all big droplets impact on the wall of the spray chamber. This is effectively done by a cyclonic spray chamber, which is depicted in figure 2.6 b). The reason for avoiding big droplets is, that they could extinguish or at least cool down the plasma significantly, which would result in unstable ionization conditions.

A big advantage of liquid analysis is, that through the process of sample preparation a lot of unwanted and disturbing matrix can be removed and the sensitivity and accuracy of the measurement is improved. Furthermore the quantification in liquid ICP-MS is fairly easy, because for nearly all elements certified reference solutions are available. But this way of sample introduction has some drawbacks too: Solid samples must be dissolved prior to analysis and thereby spatial information of analyte distribution is lost and the handling is quite prone to errors.

Solid Sample Introduction: Laser Ablation

To prevent a maybe tedious and error-prone sample preparation of solids and to keep potentially spatial information, it is possible to use laser ablation for sample introduction. The laser beam is focused on the surface of the solid sample. The energy of the laser is high enough to vaporise the sample and particles in the scale of nm are formed. These particles are transported into the torch of the ICP-MS with a He stream. The spot size of the laser can be varied from several µm to some hundred µm and the MS signal can be linked to the local position of the laser beam. Thus, by moving the sample it is possible to get spatially resolved information about the sample. With appropriate software the signal intensities are converted into colour scales and images of the sample can be created. The drawbacks of a labour-intensive quantification and higher standard deviation should be concealed.

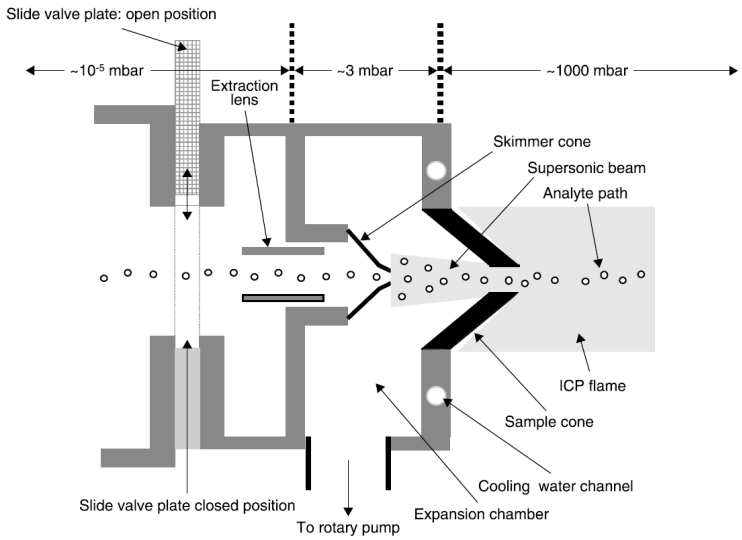

FIGURE 2.7: Schematic diagram of an ICP-MS sample interface to surmount the pressure difference from ambient pressure at the plasma to high vacuum at the mass analyser and ion detector. [20]

2.2.4 Sample Interface

After transformation of the sample into small particles or droplets with the above described methods, ions are produced in the plasma torch. The plasma is operated at ambient pressure whilst the mass analyser and the ion detector operate at high vacuum (10^{-5} - 10^{-7} mbar). Otherwise the mean free path of the ions would be too short for sufficient ion transmission. A big pressure drop (10^{8} - 10^{12} mbar difference) within a few cm thus has to be surmounted. This is accomplished by an interface design, which is depicted in figure 2.7. The main parts of this interface are two cones usually made out of Ni alloys. These cones have narrow apertures to prevent the collapse of the high vacuum. The first cone, which is called sample cone has an aperture diameter of 0.5 to 1 mm. The first vacuum step (low mbar pressure) behind the sample cone is established with an rotary pump. The second cone, called skimmer cone (0.5 mm aperture diameter), separates the high vacuum zone from the mid vacuum in the expansion chamber. The high vacuum is usually maintained by a turbomolecular pump.

As the ion beam travels through this interface, broadening of the ion beam and consequently a loss of ions occurs. As Liezers refers in [20], from one mio. ions produced in the plasma, only one single ion can be detected. All other 999 999 possible ions for detection get lost on their way from the plasma torch to the detector.

2.2.5 Collision Cell

Before the ion beam enters the mass analyser, there is the possibility that the ions are sent through a collision cell. This is a device to suppress isobaric interferences, meaning two ions with more ore less the same masses. This function can be switched

on and off manually. Collision cells are effective in filtering polyatomic ions from monoatomic ions with similar $\frac{m}{z}$-values. These collision cells contain for example a quadrupole mass analyser and some collision gas (e.g. H_2 or He). The incoming ions accelerated to a certain kinetic energy (e.g. 20 eV). As the ions travel through the collision cell, they collide with the gas molecules. The bigger their collision cross section is, the higher the chances of colliding with gas molecules. During a collision event, kinetic energy is transferred from the moving ions to the as stationary considered gas molecules. Imagine two ions with nearly identical masses, but different size. At the end of the collision cell, the bigger ion will have less kinetic energy, than the smaller one. A potential barrier at the exit of the cell will block the ions with lower kinetic energy. Provided that a polyatomic ion has a larger cross section than the monoatomic ion with the same mass, it is possible to hinder the polyatomic ion from reaching the detector [22].

2.2.6 Mass Analyser and Detector

Mass analysers are devices, which are capable of discriminating ions because of their mass over charger ratio ($\frac{m}{z}$). A widely used mass analyser for inorganic mass spectrometry is a so called quadrupole analyser. It consists of four parallel, metallic rods. Two rods form a pair and exhibit the same polarity. Additional to this direct voltage a high frequency alternating voltage is applied to every pair of rods with 180° phase shift respectively. A schematic drawing is given in figure 2.8 a). The trajectory of the travelling ions is influenced by the electrical fields generated by the rods. If the polarisation of one pair of rods is lower than the potential of the ion, the ion will be attracted, otherwise repulsed. How much the trajectory is influenced depends on the mass of the ion, the frequency of the alternating voltage and the amplitude. High masses will be slightly influenced by high frequency or low amplitude of alternating voltages, due to their inertia. Whereas light ions will already be influenced by this kind of alternating voltages. This influence of the trajectories causes the ions to strike the rods, where the ions are discharged and are lost for detection. At a given frequency only a single $\frac{m}{z}$-value is able to pass the mass filter.

The ions which pass the mass filter are detected at a device which is able to determine the amount of incoming ions in a certain period of time. In figure 2.8 b) the general working principle is depicted. When the so called conversion dynode (Cu-Be alloy) is hit by an energetic ion, at least two electrons are formed. These electrons are attracted to the next diode by electrostatic forces, where again more electrons are emitted than impinging. This process happens several times to create a measurable electron current from a single ion impact. As seen in figure 2.8, there is a discrete and a continuous design possible. Nowadays so called microchannel plates are commonly used. These microchannel plates contain many miniaturised continuous-dynode electron multipliers with the big advantage of simultaneous detection of multiple incidents and improved precision [18].

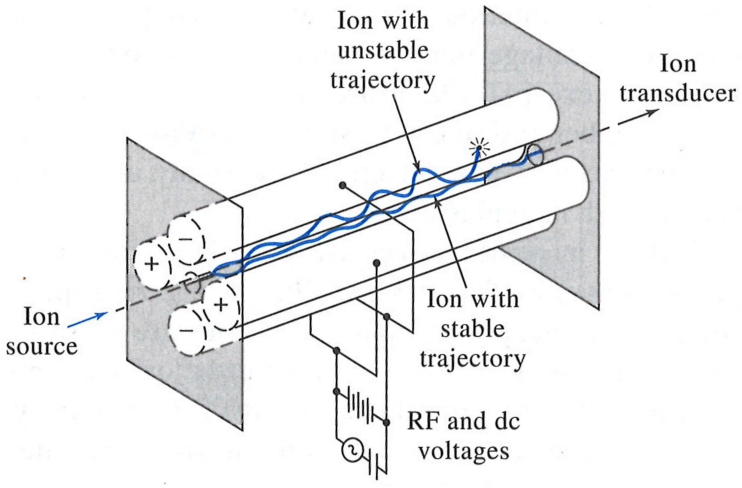

(a) Schematic drawing of a quadrupole mass analysator; at given set of direct and alternating voltages, just one $\frac{m}{z}$-value is able to pass the analyser. All other ions will impact on the rods and be discharged.

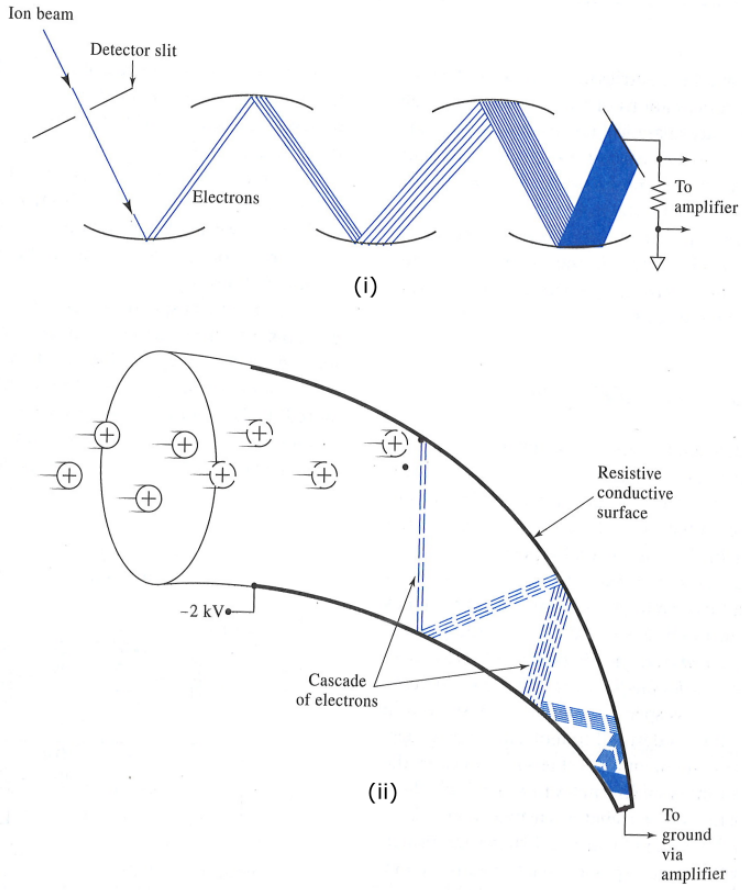

(b) Electron multipliers in discrete-dynode design (i) or continuous-dynode design (ii);

FIGURE 2.8: Elements used in ICP-MS for analysing $\frac{m}{z}$-values and detection of the ions; [18]

2.3 Pulsed Laser Deposition

2.3.1 Principle

Pulsed laser deposition is a versatile method for the preparation of novel multi-elemental or multi-layer thin films of high quality [23, 24]. It is described as a promising technique for the formation of complex-oxide heterostructures, superlattices, and well controlled interfaces [25]. The principle idea behind it is briefly explained: A laser beam is focused onto the surface of the target material. The energy of the laser pulse is high enough to form a plasma and to vaporise a small amount of the target. The material removed from the target is deposited on the surface of the substrate. This process is depicted in figure 2.9. It has to be mentioned that film growth can hardly be predicted on a quantitative basis, since the interplay of the active physical precesses is highly complex and effects of all relevant parameters are not studied in detail. In the following some crucial processes and their influence on the physical behaviour of the deposited thin film shall be described in more detail.

2.3.2 Interaction of Radiation with Matter

When a laser beam with a pulse duration in the range of ns and with sufficient energy hits the target, some surface atoms will be ionised due to the large electric field of the focused light. Usually the radiation is absorbed in the first 10 nm of the solid. The removed electrons will start to oscillate in the electromagnetic field of the light and thus create further ions and electrons by collision, if the energy input of the laser is high enough. This process leads to the formation of the so called plasma plume, which contains atoms, molecules, ions, and free electrons in varying ratios. The overall process is called laser ablation.

As mentioned above one should be careful about the mechanistic processes on the irradiated surface. As remarked in the work of Miotello and Kelly [26, 27], the process is not merely a melting and vaporising of the material as one would imagine. Depending on pulse duration and used energy, the reactions at the solid surface with the radiation can vary. Due to the fast rise of the temperature, a so called phase explosion is reached, which leads to a rapid transformation from solid state to a mixture of vapour and liquid droplets. Due to this fast process it is assumed, that no phase separation can occur in the bulk material. This is an unsurpassed advantage of ablating particles with photons compared to other ablation techniques.

The plasma plume created this way will expand and be repulsed from the target because of coulomb forces. At the heated substrate the material is deposited and is expected to form a thin film with desired stoichiometry. Willmott [23] reports that films produced by non-thermal processes like PLD will more likely have the same stoichiometry as the target. Especially multi-element containing oxides (such

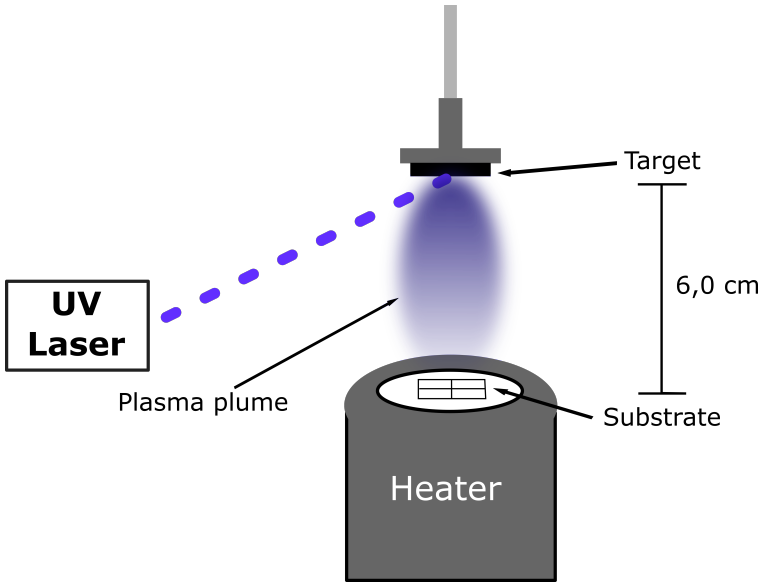

FIGURE 2.9: Schematic diagram of the PLD process: UV-laser radiation generates a plasma plume containing atoms, ions and electrons. Thin films are deposited on the surface of the substrates.

as doped perovskites) are hard to deposit with correct stoichiometry by thermal deposition techniques, because of the different boiling points of the elements. For such multi-elemental materials PLD is an adequate synthesis method.

2.3.3 Fundamental Parameters Influencing PLD

In the review by Willmott about the deposition of complex multielemental thin films [23] four parameters influencing the quality of deposited films by PLD are discussed: (i) the substrate temperature, (ii) the laser fire frequency, (iii) the background pressure in the PLD-chamber and (iv) the energy of the atoms/ions impinging onto the substrate surface. An elevated substrate temperature allows surface diffusion of the deposited material, whilst bulk diffusion is avoided. Together with a reasonable value for the deposition rate (time between two pulses should be in the order of 100 ns) these two parameters seem to influence the film quality, because the atoms arriving (also called adatoms) at the surface need some time to find a stable low energy site. At these sites the atomic coordination number is increased. Therefore the adatoms are primarily integrated at steps of the layer which is already deposited or islands will be formed when at least two adatoms meet. The pressure in the PLD-chamber can range from high vacuum to several Pa. This background pressure influences the movement of the atoms/ions on their way from target to substrate. With high background pressure, the sputtered particles will collide more frequently with gas atoms. These collisions cause an energy transfer from the sputtered particles, which have high kinetic energies and a change in flight direction. This leads to a broadening of the plasma plume and consequently a decrease of the deposition rate. Furthermore the energy of the atoms impinging on the substrate should not be too

high, because resputtering of already deposited material is possible. This process can be suppressed by reducing the kinetic energy of the particles with the pressure of the background gas. Besides these four parameters already discussed, the author assumes, that there is at least another parameter, which is especially influencing the chemical composition of the deposited films. As discussed later on, the distance between target and substrate should not be neglected during the optimisation process.

Chapter 3

Experimental

3.1 Powder Synthesis

The powder used in the experiments of this work was synthesised at the Forschungszentrum Jülich, Germany. Via spray pyrolysis a 10 kg batch of LSCF powder for various sample preparation techniques and analysis was produced. Therefore the nitrate salts of each cation were weight out in the correct proportion and dissolved. The solution is sprayed into a hot gas stream. The resulting powder is calcined and ground subsequently to reach a particle size distribution with a median diameter d_{50} = 0.8 µm. The targets with 1 cm in diameter and 1 mm thickness are produced in a stepwise pressing procedure: At first 1 g of the powder is pressed uniaxially with 200 MPa and secondly a cold isostatic pressing step with 300 MPa is executed. Afterwards the disc is sintered at 1250 °C. The target is fixed to the target holder with a two-component-adhesive (Duralco 4700HT, Cotronics Corp., USA).

3.2 Thin Film Synthesis

For depositing thin films of LSCF a PLD equipment similar to the one described in section 2.3 was used. A KrF excimer laser (λ = 248 nm, Lambda COMPexPro 201F) operated at a repetition rate of 5 Hz and 50 ns pulse duration with approximately 1.5 J cm^{-2} laser fluence was source of radiation. As substrates, yttrium stabilised zirconium dioxide single crystals (YSZ, 9.5 mole% Y_2O_3) with 5 x 5 mm in size and 0.5 mm thickness purchased from Crystec GmbH, Germany were used. The surface of the substrates has (100) orientation and is polished epitaxy-ready. The substrates could be recycled by removing previously deposited LSCF with concentrated HCl and were used several times after a visual check of the crystal surface in the optical microscope. If the surface showed too many cavities the substrate was not used again. As background gas O_2 with a partial pressure of 0.04 mbar was flushed through the chamber. The substrate was heated with a resistance heating based on Pt alloy wires in a corundum matrix. The surface temperature of the substrates was measured via detection of emitted infra-red radiation by a pyrometer. The sputter process was started after reaching the target value of 600 °C. An approximately 50 nm thick layer of gadolinium doped cerium oxide (GDC, 20 mole% Gd_2O_3) was

TABLE 3.1: PLD operating parameters;

Parameter	Used Values
Laser fluence	ca. 1.5 J cm^{-2}
Repetition rate	5 Hz
Pulse duration	50 ns
O_2 background pressure	0.04 mbar
Substrate temperature	600 °C
Sputter time	1 200 pulses (GDC), 18 000 pulses (LSCF)
Expected film thickness	50 nm (GDC), 200 nm LSCF)
Target to substrate distance	6.00, 6.75, 7.50, 8.25 cm

used for suppressing an unwanted formation of $La_2Zr_2O_7$ between the substrate and LSCF.

The practical procedure was the following: Before inserting the targets into the PLD chamber, a grinding step with sandpaper was executed to remove the coarse surface caused by the last ablation. Both targets (GDC and LSCF) were inserted in the manually movable target carousel at once. The clean substrates were inserted into the specimen holder and placed on top of the heater in the PLD chamber. After evacuating the chamber to 10^{-4} mbar, an oxygen partial pressure of 0.04 mbar was adjusted and the substrate heated to 600 °C. The O_2 background pressure was controlled with a mass flow controller (MFC) ensuring a constant gas flow and the vacuum system working with constant power. Both targets were pre-ablated with 250 pulses to clean the target surface and reach steady state. 1 200 laser pulses were used for depositing the GDC layer and 18 000 pulses for LSCF. As it could be shown, the distance between target and substrate is crucial for the stoichiometry of the deposited layer. This parameter was varied in the range of 6.00 and 8.25 cm with a step width of 0.75 cm. After deposition the samples were cooled to room temperature with 15 °C per minute and the chamber was solely opened below 150 °C to prevent possible surface reactions with H_2O or CO_2. All parameters and values used for PLD operation are given in table 3.1. It was taken care to be able to track the position of every single sample back to where it was positioned in the PLD chamber. Therefore the samples were denoted with LO („links oben“), LU („links unten“), RO („rechts oben“) and RU („rechts unten“). Figure 4.8 shows a picture of a sample with the specimen holder and numbered 5 x 5 samples. RO and RU are sample numbers 2 and 4, and LO and LU are sample numbers 1 and 3.

TABLE 3.2: ICP-MS operating parameters; Elements marked with * used for evaluation;

Parameter	Liquid sample introduction	Solid sample introduction
RF power	1550 W	
Auxiliary gas flow	0.8 L min^{-1}	
Cool gas flow	14 L min^{-1}	
Nebuliser gas flow	1 L min^{-1}	
Dwell time per mass	0.1 ms	
Collision gas flow	3 mL min^{-1}	
Measured Isotopes	^{56}Fe*, ^{57}Fe, ^{59}Co*, ^{63}Cu, ^{65}Cu, ^{86}Sr, ^{88}Sr*, ^{138}La, ^{139}La*	

3.3 ICP-MS Operation Parameters

For obtaining ICP-MS data the Thermo iCAP Q instrument by ThermoFisher Scientific, Bremen, Germany was used. This instrument is equipped with a quadrupole mass analyser, an auto sampler for liquid samples (ESI SC-2DXS by Elemental Scientific, Inc., Omaha, NE) and a spray chamber, which is cooled with a peltier element. For nebulisation a Meinhardt nebuliser and a cyclonic spray chamber were used like those depicted in section 2.2.3. The Qtegra software, delivered with the instrument, was used for data acquisition. For solid sample introduction the ICP-MS instrument was coupled with the LA equipment via PTFE tubes. The liquid as well as the solid sample measurements were carried out using KED-mode. All relevant operating parameters for both measurement types are summarised in table 3.2. The ICP-MS instrument was optimised with respect to a maximum of ^{115}In signal before every measurement day using either a liquid standard solution (Multi-Element TUNE A by Thermo Fischer Scientific) or a solid glass standard (NIST 162 by National Institute of Standards and Technologies, USA).

For solid sample introduction a NWR213 laser ablation system (ESI, USA) was used working with a frequency quintupled 213 nm Nd:YAG laser (4 ns pulse duration). To ensure a fast washout behaviour an ablation cup, which is positioned above the ablation spot, is installed. Due to better results in the particle formation process, He is used as carrier gas. Before reaching the ICP-torch, the carrier gas is diluted with Ar as make-up gas. Table 3.3 summarises the operation parameters of the LA system.

TABLE 3.3: LA operating parameters;

Parameter	Used Values
Laser fluence	0.52 J cm^{-2}
Repetition rate	10 Hz
Pulse duration	4 ns
spot size	250 µm
scan speed	750 µm s^{-1}
He carrier gas flow	600 mL s^{-1}

3.4 Sample Preparation

3.4.1 H_2O Etching

The H_2O etching procedure was as follows: 5 mL of purified water (produced by Barnstead^{TM} Easypure^{TM} II (18.2 M cm^{-1})) was added to each sample in a testing tube. After 30 min and carefully tilting the tubes twice, 4.5 mL of the liquid was transferred into new testing tubes. To prevent adhesion of the cations at the polypropylene walls of the testing tubes, the solution was acidified with 45 µL conc. HCl (37 vol%, EMSURE®, for analysis). Additionally 45 µL of a Cu solution with a concentration of 1 ppm was added as internal standard. This internal standard was used in every sample or calibration standard with a resulting concentration of 10 µg L^{-1} to detect and being able to correct fluctuations during the measurements. All volumetric work steps were weighted with a balance to get more precise data for quantification. It has to be mentioned again that with this etching procedure only water soluble substances at the surface of the sample can be detected. In this case $SrO/Sr(OH)_2$ is expected to get dissolved. The LSCF perovskite is not soluble in H_2O with neutral pH-value.

Quantification was achieved with an external calibration. Therefore single element standards for La, Sr, Co and Fe were combined in a mixed standard solution with equal concentrations. From this stock solution calibration standards with 0.2, 0.5, 0.7, 1.0, 2.0, 5.0 and 10.0 µg L^{-1} were prepared. The used standards and their certified analyte contents are presented in table 3.4.

3.4.2 HCl Etching

For determining the complete stoichiometry, the whole film was dissolved with conc. HCl. Therefore the remaining 500 µL H_2O in the first sample tube was removed and 100 µL conc. HCl was added to the dry sample. Afterwards the conc. HCl was diluted with 8 mL of 1 vol% HCl. An aliquot of 500 µL is taken from this solution and mixed with 4.5 mL 1 vol% HCl to obtain a sample solution with concentrations in the range of 10 to 150 µg L^{-1}. Cu is added as internal standard as

TABLE 3.4: Used certified standard solutions acquired from VWR INTERNATIONAL LTD;

Element	Certified value [mg kg^{-1}]	Product No.	Lot No.
Fe	1000 +/- 0.5 %	455522V	B9025042-1A
Co	1000 +/- 0.5 %	455262U	B9035124
Sr	1000 +/- 0.5 %	4560625	210085030
La	1000 +/- 0.5 %	455542C	214115040

described above. For quantification the same standard solution mix was used to produce standards with 10, 20, 50, 70, 100, 120 and 150 µg L^{-1} analyte.

3.5 Annealing Experiments

For investigating the Sr segregation behaviour, samples were annealed in a tubular furnace with adjustable atmospheres. The samples for these experiments were all produced with the optimised PLD parameters (7.5 cm substrate-target distance). As annealing temperature 800 °C with 5 °C min^{-1} heating ramp was chosen, because this is a typical SOFC operating temperature for SOFCs of the intermediate temperature regime. All four samples of one PLD batch were annealed and analysed subsequently with ICP-MS and the H_2O etching method. The furnace was fed with two different gase mixtures - synthetic air and humidified synthetic air. The synthetic air used is a mixture of N_2 (80 %) and O_2 (20 %) containing less than 3 ppm H_2O. For the humidification the synthetic air was flushed through a system of three cylinders where the one in the middle was filled with water and a glass frit. By bubbling gas through the water, it is assumed that the synthetic air takes up H_2O to its equilibrium. The water vapour pressure for 20 °C gives 2.3 vol% H_2O in the gas stream. This gas is denoted afterwards as humid synthetic air.

3.6 Creating an Image of a LSCF Film by LA-ICP-MS

For the imaging experiment an Al_2O_3 substrate with a diameter of 4.5 cm was produced covering the whole area of the substrate heater. This substrate was cut and polished in house. On top of this Al_2O_3 disc GDC as intermediate layer and LSCF at 6.0 cm substrate to target distance were sputtered. The other parameters were the same as given in table 3.1.

For data evaluation of the LA experiment, the software ImageLab by Epina GmbH, Pressbaum, Austria (version 2.48, 64 Bit) was used. With this software the time and intensity values for each element can be imported and converted into an image. Therefore it is necessary to choose an element, with a signal being always present

as soon as the laser fires and vanishes between two laser pulses. In this case La was chosen. Because of the pattern of constant signal and no signal, the software detects the lines in the data file and calculates the image. Due to the lack of suitable standards, quantification was not possible. Therefore it is necessary to form elemental ratios to overcome fluctuations during the measurement. It is important to note that the information gained this way is not quantitative. It is not possible to calculate the stoichiometry of the LSCF film at any position of the Al_2O_3 disc as it is possible with liquid ICP-MS measurements. It is only possible to state that a measured point A contains more or less of an element than a measured point B expressed in relative percentage.

3.7 Further Calculations

3.7.1 Estimating the Sr Monolayers

Due to the external calibration of the liquid measurements described above and the used software, primary information of the concentration of the analytes in the measured solution in µg L^{-1} was obtained. These values were recalculated with respect to the whole amount of the etching solution, the molar masses and eventually taken aliquots to receive comparable data. This calculation was done with the following formula for the H_2O etching (equation 3.1) and for the HCl etching (equation 3.2):

$$y_{analyte} = \frac{x_{analyte}}{M_{analyte}} * \frac{m_{supernatant}}{m_{measured}} * m_{etch\,solution} \tag{3.1}$$

$$y_{analyte} = \frac{x_{analyte}}{M_{analyte}} * \frac{m_{aliquot} + m_{1\%HCl}}{m_{1\%HCl}} * m_{etch\,solution} \tag{3.2}$$

Where the result $y_{analyte}$ is in nmol, $x_{analyte}$ is the concentration in µg L^{-1} calculated by the software, $M_{analyte}$ is the molar mass in g $mole^{-1}$, $m_{supernatant}$ is the amount of liquid taken after the H_2O etching in g, $m_{measured}$ and $m_{etch\,solution}$ are the masses in g of the actually measured solution and the amount of H_2O used for etching.

For an easier compareability the nmol quantity of Sr in the solvent calculated above is converted into monolayers of SrO covering the surface of the sample. Therefore it is assumed, that Sr is present as SrO (100) at the top of LSCF and covering the entire surface. These assumptions are made from results by Druce et al. [9], who applied Low Energy Ion Scattering on LSCF surfaces. SrO has rock salt crystal structure ($Fm\bar{3}m$) with a lattice constant of 5.16 Å (PDF Nr. 00-006-0520 (ICCD, 2010), [28]). One unit cell contains two atoms of Sr. With a sample area of 25 mm^2 0.31 nmol Sr form one monolayer of SrO. It has to be mentioned that there are hints that some LSCF is also deposited on the side of the substrates. Eventhough deposition

on the sides of the substrates may not be homogeneous, a small but measurable effect can be expectet. Therefore, Rupp et al. [3] considered a 4 % increased area at the top (26 mm^2) for their calculations. That is the reason, why their calculation (0.33 nmol Sr/ monolayer SrO) slightly differs from the one presented here (0.31 nmol Sr/ monolayer SrO). In this work all results will be calculated without correcting a possible effect of the edges. There are two reasons why this additional area is not taken into account here. First, there is no possibility to estimate the amount of LSCF deposited on the sides. The 4 % used by Rupp et al. is merely a guess and second, the concept of SrO covering the whole sample area is very hypothetical. Different Sr species, like $Sr(OH)_2$ or carbonates, and the formation of SrO islands rather than homogeneous films is possible too.

3.7.2 Calculating the LSCF Film Thickness

Film thickness of the deposited material can also be derived from the data obtained by ICP-MS measurements with following equation:

$$y_{film\,thickness} = \frac{M_{LSCF} * \frac{x_{sum\,all\,cations}}{2}}{d_{theoretical}} \tag{3.3}$$

In equation 3.3 $M_{LSCF} = 220.08 * 10^{-9}$ g mol^{-1} is the molar mass, $x_{sum\,all\,cations}$ in nmol is the sum of La, Sr, Co and Fe cations in the H_2O etching solution and the HCl etching solution together divided by two and $d_{theoretical}$ in g nm^{-1} is the theoretical layer thickness calculated with a theoretical density of 6.36 g cm^{-3} [16] for $La_{0.58}Sr_{0.40}Co_{0.20}Fe_{0.80}O_3$. The resulting LSCF film thickness $y_{film\,thickness}$ is obtained in nm. Considering the general stoichiometry of a perovskite (ABO_3), the sum of all cations has to be divided by two, since one mole perovskite contains two mole cations. Using solely the sum of either A or B type cations should theoretically be possible, but, as it can be seen in the results of the experiments, the amounts of A type cations and B type cations are not equal.

Chapter 4

Results and Discussion

4.1 ICP-MS Results of the H_2O Etching Process

4.1.1 Situation Before Improvement

At the beginning of this work, some time was spent for gaining practical routine in sample synthesis and measurement operation. The data shown here begin with PLD sample number 45. This means that 44 samples have been used for training to minimise variations due to practical fluctuations. The PLD parameters used at the beginning based partially on empirical observations. Therefore it was necessary to collect data of the status quo. 16 samples were produced consecutively and measured in one run. The ICP-MS results for the H_2O etching experiments are shown in figure 4.1. This bar chart shows the amount of La, Sr, Co and Fe cations found in the H_2O etching solution. Four samples are produced in one PLD run. These different runs are denoted as batch 1 to 4. The results for Fe cations are usually below detection limit (LOD). The values for La and Co are significantly above LOD. The obtained LOD values for the measured cations are usually 0.03 ppb or lower. However the focus of this H_2O etching experiments lies on the Sr values.

In the next paragraph, the different levels of standard deviations shown in figure 4.1 are explained in more detail. The errorbars of every single cation result from four main runs of the ICP-MS measurement and are calculated by the software. The quality of the four main runs was already checked at the point of measurement. These bars represent the fluctuations of the ICP-MS equipment during the measurement time of one sample and are negligibly small. In the next level the RSD value of the four samples of one batch is calculated and is denoted below the x-axis. The RSD values for the four batches vary from 9 to 18 %. These values are astonishingly high because it is assumed, that the four samples produced in one PLD run are identical and thus can be treated as replicates for the ICP-MS measurements. Replicates usually exhibit 2 to 3 % RSD in this kind of measurement set up. The average over all 16 samples is 0.29 nmol with 15 % RSD, which is depicted with a bold dashed line and a fine dashed line in figure 4.1, respectively. As described in section 3.7 this amount of Sr represents nearly one monolayer of SrO depicted on the right y-achsis, which is in good agreement with literature [12, 29, 30].

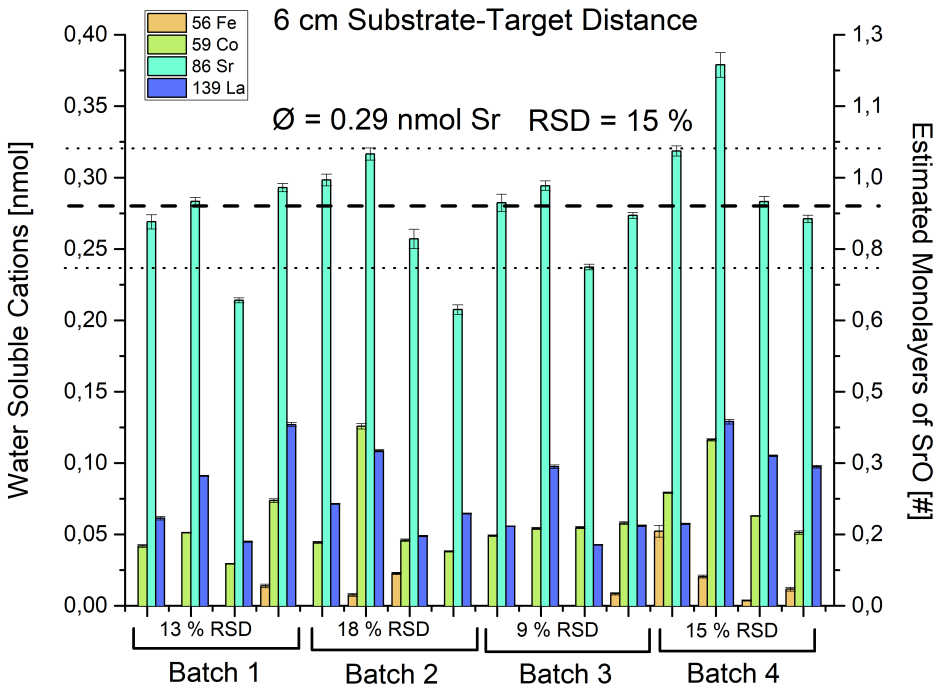

FIGURE 4.1: ICP-MS results of the cation amount in the H_2O etching solution for 16 samples produced all with the same common PLD parameters showing high RSD values. The average and the RSD values given are always calculated with respect to the Sr amount.

Furthermore, in this bar chart some weak pattern of water soluble Sr amount can be detected. For example, the 3^{rd} bar of every batch is much lower than the first two bars. During sample synthesis it was taken care of the individual position of every sample. Thus, the third bar represents a sample positioned at the same spot in the PLD chamber. This can be interpreted as a hint that there is some lateral variation caused by the PLD process and four samples of one batch may not be considered as equal. This idea of lateral variations caused by the PLD process will be investigated in further experiments - see section 4.3.

4.1.2 Variation of PLD Parameters to Minimise Fluctuations

With the aim of minimising the variations of the amount of water soluble Sr, two PLD parameters were investigated. The first parameter varied in the PLD process was the amount of deposited material by varying the sputter time at a given laser frequency which quickly showed no significant influence on the fluctuations of the amount of water soluble Sr. The next one tested was the substrate to target distance which is basically the travelling distance of the ions and atoms in the plasma. The most commonly used distance value for depositing LSCF was 6.0 cm. With a step width of 0.75 cm the distance was increased to 8.25 cm and the values for the amount of water soluble Sr are shown in figure 4.2 a). In this chart only the averaged Sr value of all four samples produced in one PLD run is shown respectively. The errorbars in

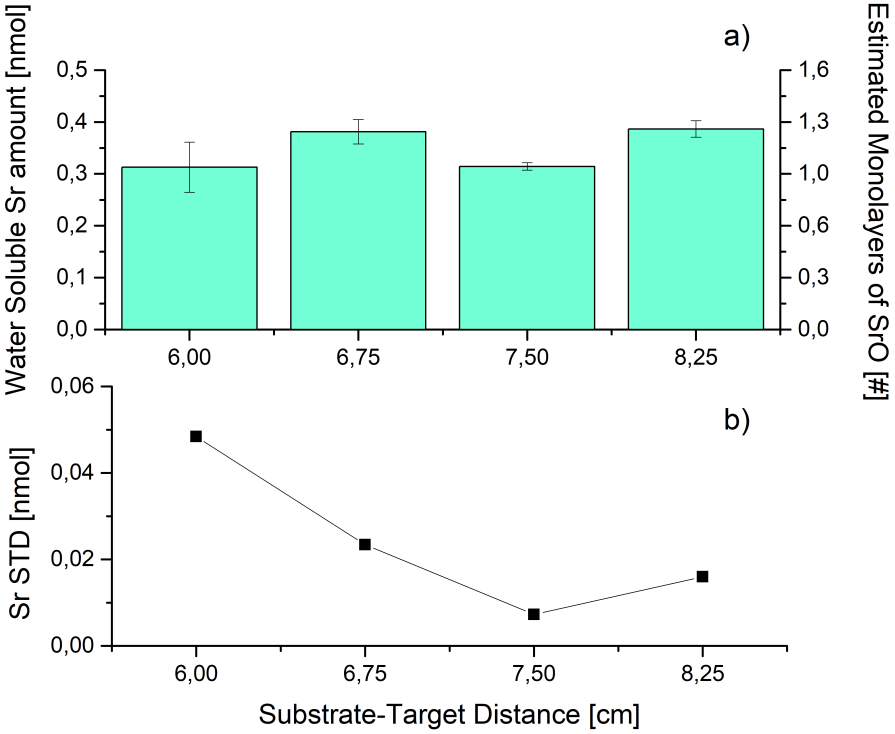

FIGURE 4.2: ICP-MS results for Sr cation amount in H_2O varying the substrate-target distance a). Average and STD is taken from four samples of one PLD batch at one distance. STD plotted against substrate-target distance showing a minimum at 7.50 cm b).

this chart represent the variations of four samples produced in one PLD run and not the variation during the ICP-MS measurement. Additionally in the lower part b) the standard deviation of the Sr values of four samples of one batch is plotted against the substrate-target distance. It can be clearly seen that there is a minimum of deviation at 7.5 cm. This minimum represents 3 % RSD which is five times lower than the starting value of about 15 % RSD. To prove significance, a one-tailed F-Test is executed with the values obtained at 6.0 cm and 7.5 cm distance showing that the variance of samples with larger distance is smaller. The null hypotheses H_0 that the variance of the first test sample (6.0 cm substrate-target distance) is smaller than the variance of the second test sample (7.5 cm substrate-target distance) can be rejected, because the F_{test} = 44.3 is bigger than the $F_{critical}$ = 9.3 at 95 % significance level. Additionally a two sample Mann-Whitney-U-test (t-test not possible, because variances are inequivalent) gives no reason to reject the null hypotheses that the averages of this two test sets are equal (U_{test} = 7.0, U_{crit} = 1.0, 95 % significance level). This means that increasing the substrate to target distance does not effect the amount of water soluble Sr detected with ICP-MS, but significantly improves the uniformity of all samples produced in one PLD run. It is important to notice that the validity of statistical tests with very few data points may not be given. Between the two test sets of samples produced at 6.75 compared with samples produced at 7.50 cm, and samples produced at 8.25 and 7.50 cm there is a significant difference, because the

U-test values are smaller than the critical U-value ($U_{test(6.75)}$ = 0.0, $U_{test(8.25)}$ = 0.0, U_{crit} = 1.0 at 95 % significance level). This may be due to inter-day variances of the ICP-MS measurements, because the samples at 6.75 and 8.25 cm were measured on one day and show the same little bit higher Sr amount and the samples at 6.00 and 7.50 cm were measured on two other days.

4.2 ICP-MS Results of the HCl Etching Process

4.2.1 Stoichiometry of the Deposited Material

The HCl etching solution contains the completely dissolved LSCF film. The relative cation ratios of each element are depicted in figure 4.3. In this chart the nominal value of every single cation is represented by a bold dashed line. Fe and Co nearly meet the nominal values. The material investigated should have 80 % Fe and 20 % Co on the B-site of the perovskite and 58 % La and 40 % Sr on the A-site. The A-sites are thus not completely occupied for stability and performance reasons. If this material is dissolved, the vacancies can not be measured. Therefore the B-site stoichiometry has to be recalculated in a way that 59.2 % La and 40.8 % Sr are the new nominal values. Sr and La on the contrary do not meet the nominal values at all. Sr is always deposited too less and La is deposited too much. Furthermore there is a trend observable which is again depending on the substrate to target distance. The bigger the distance, the less Sr and the more La is deposited on the substrate. With common PLD parameters at 6 cm substrate-target distance, the Sr amount is about 6 % lower than expected. At the largest distance, only 87 % of the nominal value is deposited. These results indicate that the substrate to target distance has a crucial influence on the stoichiometry of the produced films. The Sr amount in the thin film changes roughly with 1.3 percentage points per cm distance difference.

This trend in the individual results can also be observed, if the relation between A-site cations an B-site cations is investigated. As described in section 2.1.3 in general the A to B ration should be 1. In this case there are is a little surplus of B cations for stability and performance reasons resulting in a slight A to B mismatch of -1 %. This relative A to B mismatch is calculated by the following equation 4.1.

$$cation\,mismatch = \frac{(Sr + La) - (Fe + Co)}{(Fe + Co + Sr + La)} * 100 \tag{4.1}$$

As it can be seen in figure 4.4 at the shortest distance of 6 cm, there is a surplus of B cations close to the value of -1 % as expected. As soon as the substrate-target distance is increased, the balance flips to the side of A cations. Furthermore, the imbalance is increased when the distance is enlarged. This can be statistically proved with 15 A/B ratios at 7.5 cm (only four data points shown in figure 4.4) compared with four A/B ratios at 8.25 cm and a two sample U-test. The null hypotheses that

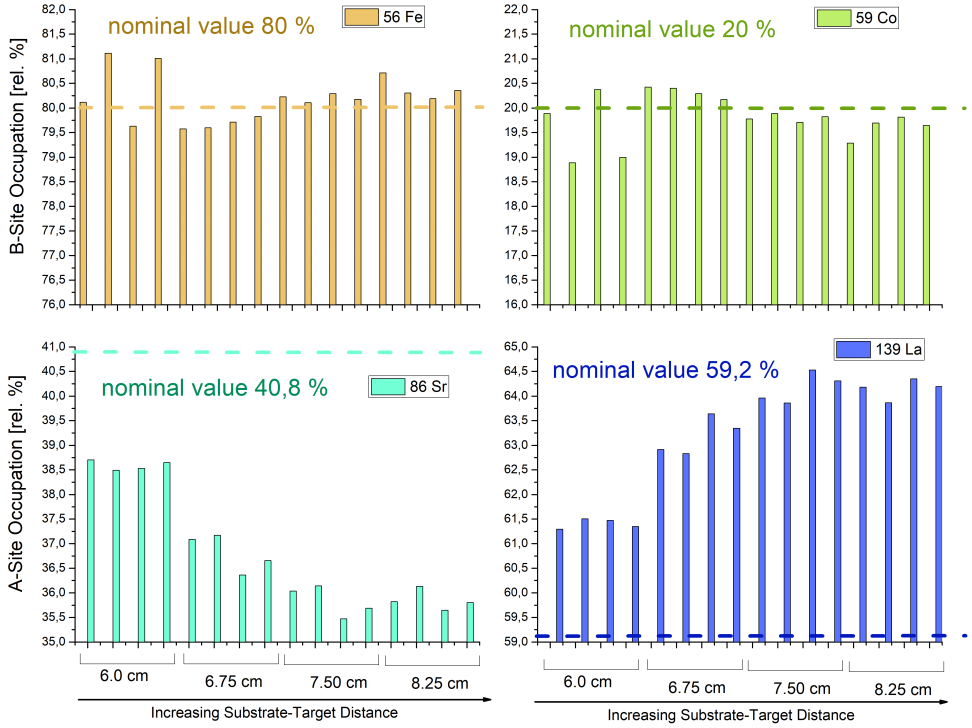

FIGURE 4.3: ICP-MS results of LSCF thin films completely etched with HCl. Results shown for every single cation.

the average of the 15 samples at 7.5 cm is equal to the second test sample (at 8.25 cm) can be rejected, because $U_{test} = 0.0 < t_{crit} = 17$ at 95 % significance level.

4.2.2 Estimating the Film Thickness

Estimating the amount of deposited material can be very tricky if the layer thickness is in the range of some hundred nm. An easy approach is to use the quantitative information given by the HCl etching experiments. As described in section 3.7.2, with additional information like theoretical density $\rho_{theoretical}$ and the molar mass M(LSCF), it is possible to estimate the thickness of the LSCF film. The results for the distance variation are shown in figure 4.5. In the upper part a) of this chart, a stacked bar chart represents the summation of the measured cation amount of every single sample (left y-axis). The right y-axis shows the calculated film thickness of LSCF. About 150 $\pm$ 9 nm LSCF is deposited on samples at 6.00 cm substrate-target distance, which is a little bit lower than the expected value of 200 nm known from previous work. In the lower part b) the averaged values of the layer thickness is plotted against the substrate to target distance. As expected the amount of deposited material decreases with increasing distance. With the first distance step from 6.00 to 6.75 cm the amount of deposited material is nearly bisected (80 $\pm$ 3 nm LSCF at 6.75 cm distance). Afterwards the decrease is not that steep.

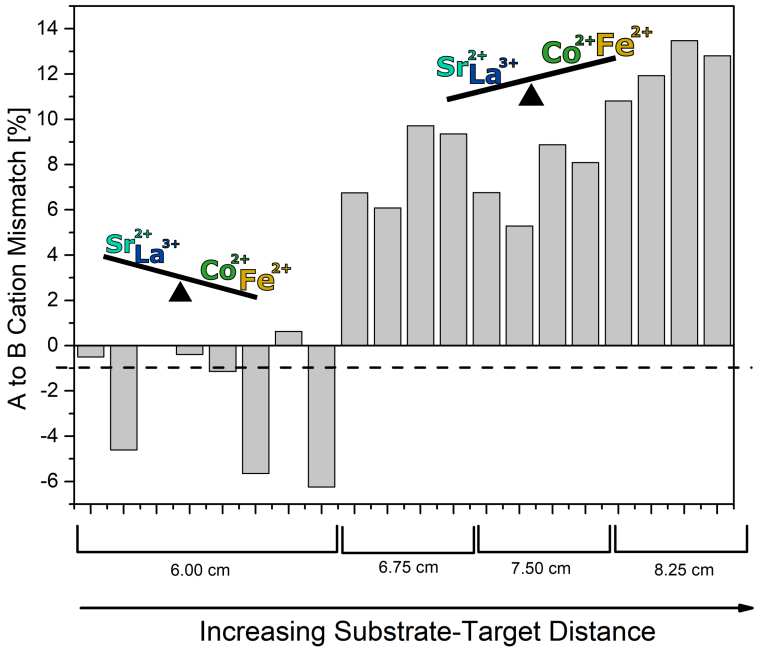

FIGURE 4.4: Mismatch of A to B cations; For an ideal perovskite the mismatch would be 0, but for the investigated composition it should be - 1 % calculated with equation 4.1.

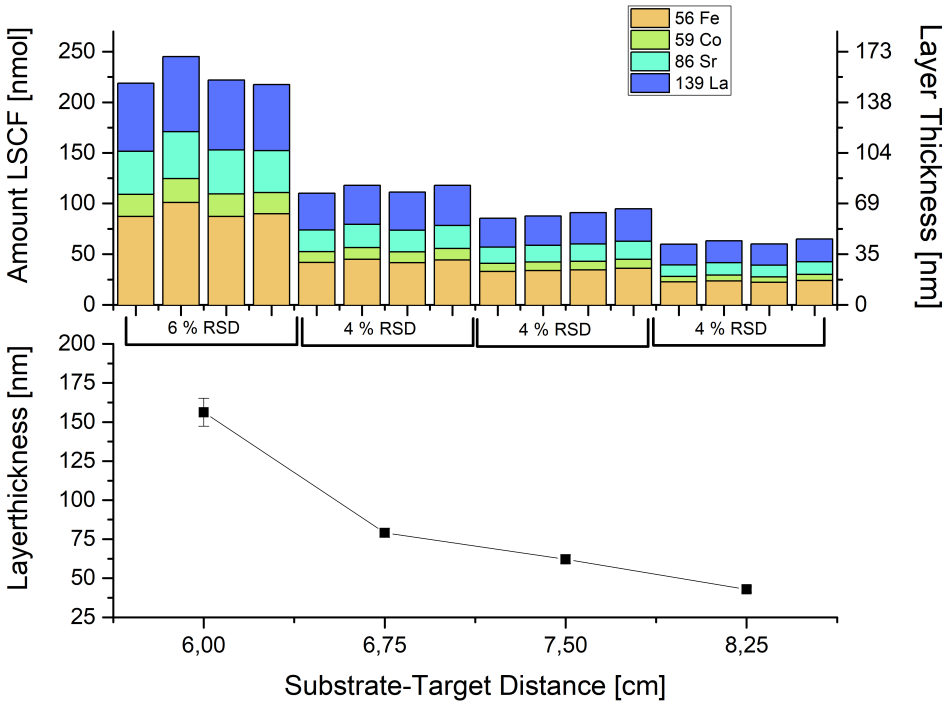

FIGURE 4.5: Estimated film thickness of the deposited material calculated with the theoretical density and the molar mass of LSCF a). Average values with standard deviation given with error bars of four samples of one PLD process b).

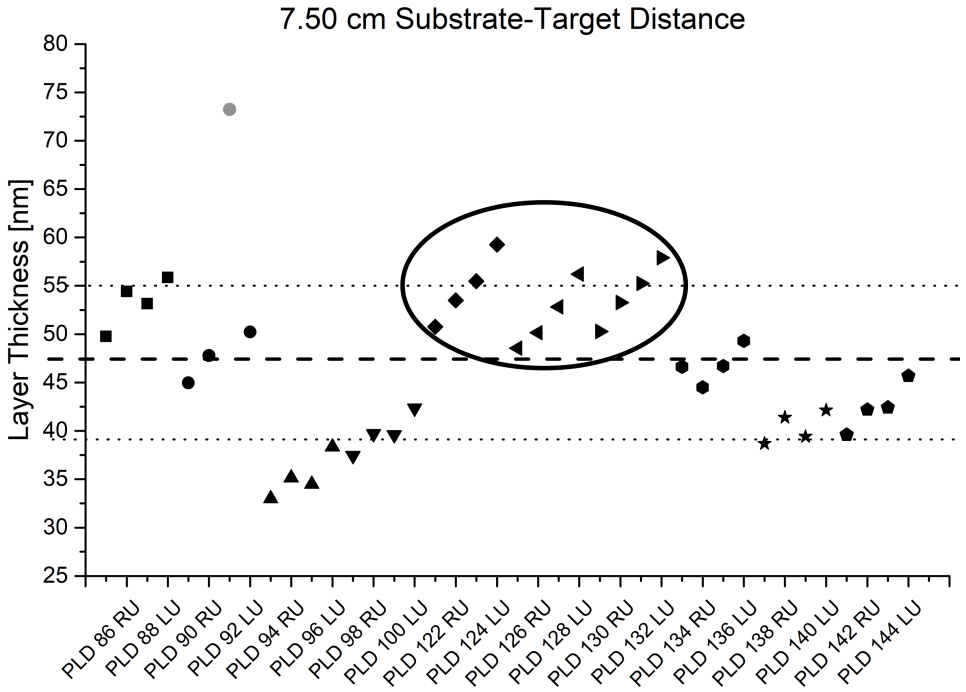

FIGURE 4.6: Estimated LSCF layer thickness of 40 samples deposited at 7.50 cm substrate to target distance. Prominent pattern visible at the samples marked with a circle. Original sample name at the x-axis to prove position sensitivity. Way of labelling is explained in section 3.2.

When looking at the amount of deposited material, some pattern among four samples of one batch is also observable. The pattern is especially prominent visible at the samples marked with a circle in figure 4.6. This can again be seen as a hint that the deposition may not be homogeneous over a sample size of 1 x 1 cm. A reason, why not all PLD batches show the same pattern could be, that positioning the target and the substrates in the PLD chamber differs to some extend from bath to bath. Monitoring the amount of deposited material over a longer period of time also revealed an average LSCF film thickness deposited at 7.50 cm substrate to target distance of nearly 50 nm with a RSD value of 17 %. The bold dashed line and the fine dashed lines represent the average and the upper and lower limit of standard deviation in figure 4.6.

4.3 Investigating Elemental Separation of the PLD Process

In the presented data so far, several hints for lateral inhomogeneity caused by the PLD process can be found - either in the elemental composition as well as in the amount of deposited material. As the atoms and ions of the plasma plume originate from a very small spot of the target (roughly a square of 3 times 1 mm), the plasma plume expands quite rapidly to dimensions of several cm. It seems that not every element has the same trajectory to travel the distance from target to the substrates.

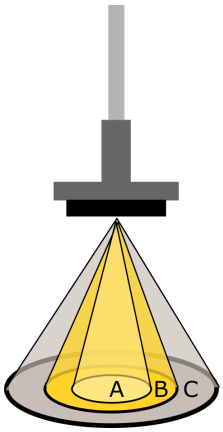

FIGURE 4.7: Schematic drawing of elemental separation in the plasma plume;

These plasma plume dynamics are discussed to play an important role in thin film quality. A very simple model to depict this process is shown in figure 4.7. Three different elements A, B and C travel with different angles from target to substrate. This may be caused by different masses and thereof resulting different $\frac{m}{z}$-values and different ion densities. In the simplest way, the heaviest element stays in the center and pushes the lighter elements off the center. This scenario is sketched in figure 4.7. On the substrate surface a ring-like structure could be expected. However, it should be noted that there are many other forces which can influence the trajectory of the ions and atoms. For example movement of the molecules of the background gas or the surface of the target may not be perpendicular to the surface of the substrate.

There are several publications dealing with this topic and revealing that thin films synthesised with PLD do not necessarily have the same stoichiometry as the target [31–37]. For Schou [36] it is even „[...] *surprising that such a high degree of stoichiometric transfer can be achieved* “. In these publications the thin film stoichiometry is usually characterised by energy dispersive spectroscopy (EDS), x-ray photoemission spectroscopy (XPS) or Rutherford backscattering (RBS). For all these publications, it was not possible to deliver a 2-D image of the elemental distribution of the sample. Whereas, with LA-ICP-MS it is possible to get spatially resolved data of the elemental composition and this will be shown in the following section.

4.3.1 Results of LA-ICP-MS Imaging

For this experiment a different kind of sample was prepared compared to the ones used in the above described data. An Al_2O_3 disc with 4.5 cm in diameter was polished and prepared so that it completely covered the substrate heater. This is the largest sample which can be produced in the current PLD set up. The resulting sample is shown in figure 4.8. The white drawing represents the original specimen holder for the 5 x 5 mm samples usually used. The four samples are denoted with 1 to 4 for an easier explanation in the text. The corresponding labelling used during

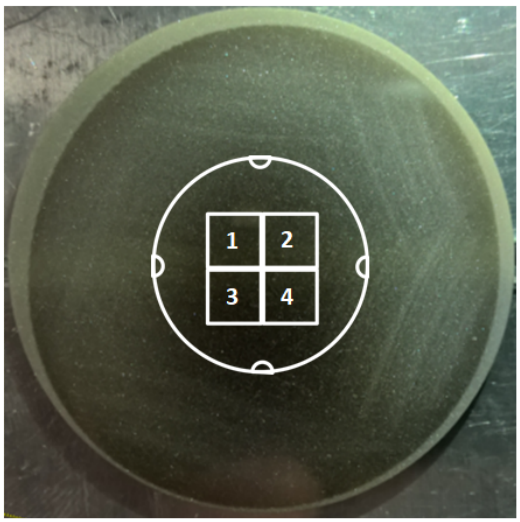

FIGURE 4.8: Sample for LA-ICP-MS measurement: Al_2O_3 disc with 4.5 cm diameter sputtered with GDC and LSCF with common PLD-parameters. White drawing represents specimen holder for common 5 x 5 mm samples used elsewhere.

the experiments is explained in section 3.2. The LA parameters given in table 3.3 were chosen in a way that the LSCF film was completely ablated. This is ensured by observing an Al signal in the mass spectrum which results from the Al_2O_3 substrate.

Before presenting the images created with the LA-ICP-MS method explained in section 2.2.3, it has to be mentioned that the values obtained are only relative differences in percentage. This is due to the lack of available standard materials which could be used as an external calibration. Therefore the ratios of all element combinations have been calculated and the changes in these ratios are depicted in the images in figure 4.9. From the colour scale beneath every image it is only possible to claim that e.g. spot 1 has 10 % more of one element or less of the other element. There is no information in this images about absolute quantities and element occupation of A or B sites as it was obtained by the liquid measurements.

Nevertheless the images depicted in figure 4.9 give an overview of an enrichment or a depletion of elements over the whole sample area which could not be seen in literature before. In case the sample was homogeneous, the whole area should be green. Yellow indicates a depletion and blue an enrichment of the element which is used as numerator to form the ratio. This colour scheme is used, because it is also interpretable if no colours are used in printing and it does not lead as easily to misinterpretations as a rainbow scale would do [38].

In figure 4.9 a) the Sr to La ratio is depicted. First of all, the dark blue area marked with the Roman number I is easy detectable. This area shows more than 10 % Sr

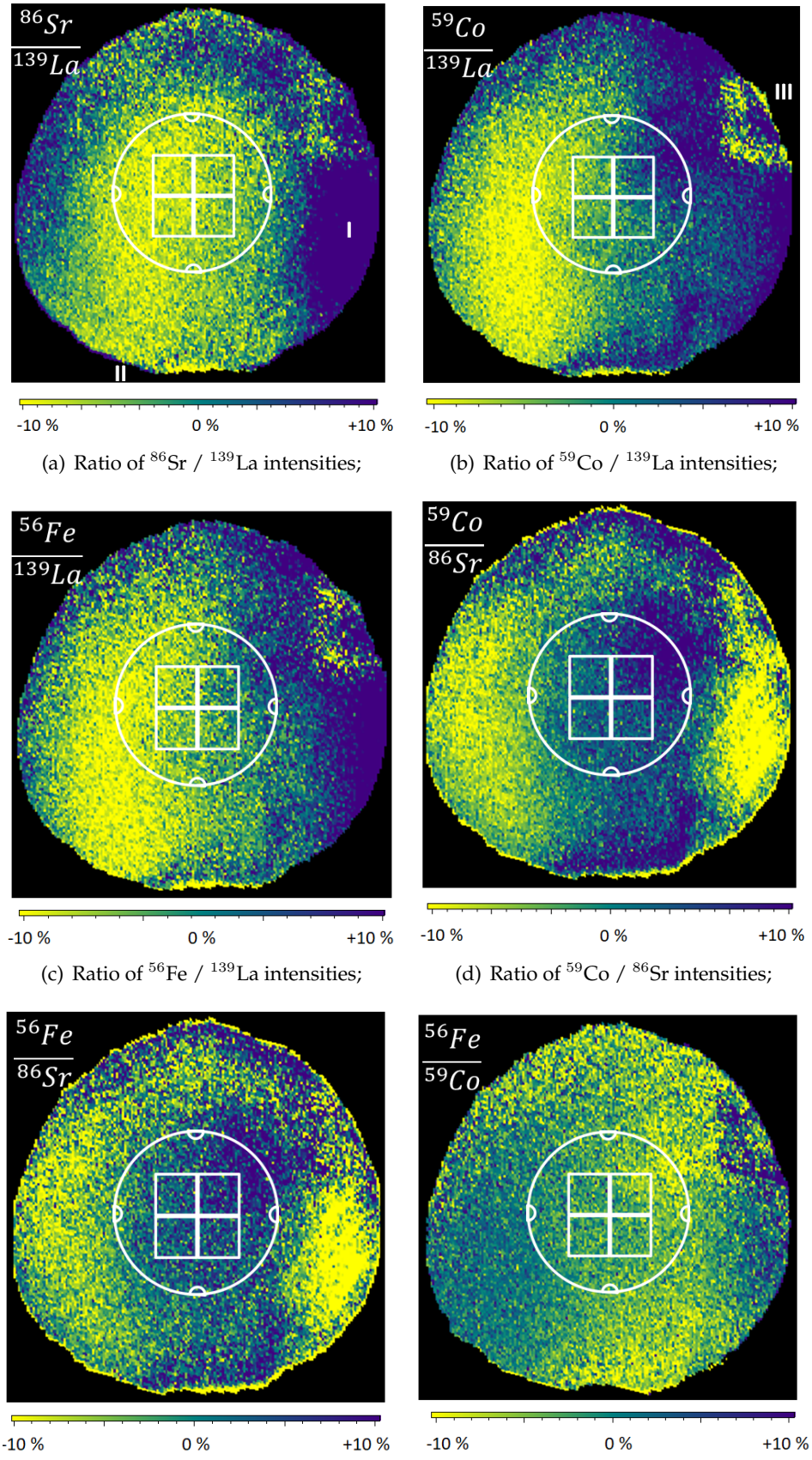

(a) Ratio of ^{86}Sr / ^{139}La intensities;

(b) Ratio of ^{59}Co / ^{139}La intensities;

(c) Ratio of ^{56}Fe / ^{139}La intensities;

(d) Ratio of ^{59}Co / ^{86}Sr intensities;

(e) Ratio of ^{56}Fe / ^{86}Sr intensities;

(f) Ratio of ^{56}Fe / ^{59}Co intensities;

FIGURE 4.9: 2D-images of spatially resolved LA-ICP-MS measurement of LSCF sample with 4.5 cm diameter.

surplus. This surplus in picture a) is vice versa noticeable as a depletion of Sr in pictures d) and e). Furthermore there is a U-shaped area with an enrichment in Sr at the border of the sample visible in picture a). The open part of the U-like structure is marked with II. The center of the sample and the area marked with II shows a depletion in Sr of about 10 %, or in other words, shows an enrichment in La. As described above for the simple idea of elemental separation given in figure 4.7, the heaviest element stays centred, whereas the lighter element is pushed off the center. As it is clearly visible, there is no continuous ring of Sr enrichment in picture a), thus, additional driving forces leading to some elemental separation must be present in the PLD chamber.

At first it has to be mentioned that the shape of the laser at the target is not a circle, but a rectangle (i). It is possible that in figure 4.9 a) the rectangular shape of the laser spot is depicted. Due to the fact that the target is not precisely in center above the substrate, the rectangular could not be depicted completely. The spreading of the elements can further be explained by their charge density (ii) for ions and by collisions with background gas molecules for atoms (iii). At every collision event, kinetic energy will be transferred and the trajectory will be influence. The lighter the atoms are, the greater is the influence of the trajectory by collisions with gas molecules. This could be an explanation why La stays centred, whereas Sr is pushed further outside. An additional but minor effect could be the constant movement of the background gas (iv). To ensure a specific partial pressure of O_2, a certain flow of oxygen is ensured with a mass flow controller and the vacuum system. This implies a preferential flow direction of the gas molecules form the nozzle of the mass flow controller to the entrance of the vacuum system. Usually the velocities in the plasma plume are much higher than the ones of the gas molecules, so that this effect should be negligible small, but further calculations are necessary to compare the velocities of the background gas molecules with the atoms and ions in the plasma plume.

Part b) of figure 4.7 shows the Co to La ratio. In this picture a ring-like structure is not visible. At this picture more a partitioning of the sample in Co rich and La rich is visible with an unexpected structure in the upper right corner marked with III. There is no explanation yet for this very local half ring-like structure of La enrichment. Part c) gives a similar picture: On the left side, there is an enrichment of the heavier element and on the right side the lighter element Fe is enriched.

The parts d) and e) show both a ring-like structure where the lighter element is depleted. In picture e) a more or less yellow ring surrounds a blue center. The last ratio between the two lightest elements in part f), which also have very similar masses, does not show very pronounced areas of yellow or blue. Most of the area is green, which means that there are no big differences in the distribution of Fe and Co. Over the whole sample these two elements are mostly homogeneously distributed.

Looking at these images, the conclusion could be that the mass difference between the elements plays a certain role in the distribution over the sample area.

More important than the overview over the whole sample area, is the area of the samples which are usually investigated when four 5 x 5 mm samples are produced. These samples are depicted with the white drawing in the images and in many cases at least one of the 5 x 5 mm sample has a different colour than the other ones. This behaviour is pronounced in part b) of figure 4.7 where sample 2 is nearly dark blue and the other samples are green or yellow. This means that there is a deviation of less than 20 % in the Co to La ratio. In parts c) and d) it is also slightly visible that the 5 x 5 samples on the right side (numbers 2 and 4) have different elemental ratios than samples 1 and 3 on the left side. This is in good agreement with the results given in figure 4.4 where the elemental mismatch of A to B cations is shown. The mismatch of all films grown at 6 cm substrate to target distance varies from nearly 0 to -5 % (liquid measurements). That means there is about 5 % variation between samples produced in one PLD batch with the same parameters as the big sample was produced. In the images resulting from the LA-ICP-MS measurement as well at least 5 % variation between the samples of one PLD batch can be found. The LA-ICP-MS results thus support the findings in liquid ICP-MS measurements.

It seems that the high variance of water soluble Sr amount at the beginning was due to different elemental ratios between the samples. The reason why varying the substrate-target distance lead to an improvement is depicted in figure 4.10. The bigger the distance to the substrate, the bigger is the area at the center with homogeneous elemental ratios, although - and this is a very important remark - the stoichiometry of the film is not the same as the target. Varying the distance results in conical sections at different heights. The nearer the substrate to the target, the likelier it is that two elemental regimes are deposited on the substrates. The farer away, the bigger the area of the central element regime, which covers all four 5 x 5 samples. This situation is depicted in figure 4.10. By increasing the substrate to target distance, homogeneity at the area of four samples is won, but at the cost of stoichiometry loss.

4.4 Investigating the Sr Segregation Behaviour

4.4.1 Annealing Experiments

Considering the findings gained in the above described experiments, investigation of the Sr segregation behaviour was carried out. All samples therefore were produced at optimised PLD parameters with 7.5 cm substrate to target distance. The two different gas mixtures used are explained in section 3.5 and are herein denoted as dry synthetic air and humid synthetic air. The data obtained in this part of the

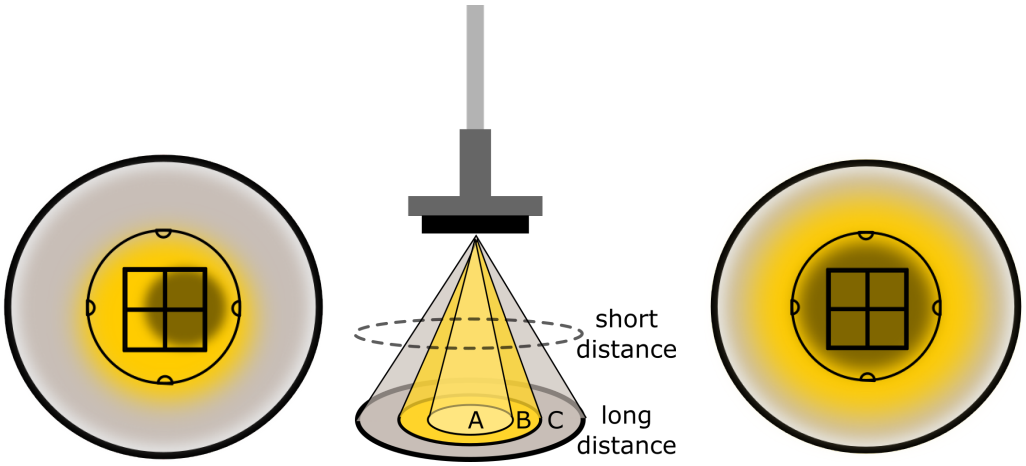

(a) Deposition pattern with short substrate to target distance;

(b) Frontal view of plasma plume and different substrate to target distances;

(c) Deposition pattern with long substrate to target distance;

FIGURE 4.10: Different projections of the influence of the substrate to target distance on the deposition pattern.

work is important for the co-workers in the Christian Doppler Laboratory, because Sr segregation has a huge influence on the degradation behaviour of LSCF cathodes and performance loss of SOFCs during usage.

In figure 4.11 a) the ICP-MS results of the H_2O etching solution for the Sr amount is plotted for the first 13 h of annealing and in part b) for all 72 h of annealing. The errorbars of every single data point are obtained by calculating the standard deviation of four samples of one batch. The samples annealed in dry synthetic air show an increasing amount of water soluble Sr on the surface depending on the duration of annealing. After 12 h a steady state of 1.1 nmol Sr or 3.5 monolayers of SrO is reached. This could be proved with a sample annealed for 72 h in dry synthetic air exhibiting the same amount of water soluble Sr (see part b) of figure 4.11). Due to the elevated temperature the amount of $SrO/Sr(OH)_2$ is about 3.5 times higher as not annealed. In the following the not annealed state will be called the as prepared state. Additionally it has to be mentioned that the last two samples in dry synthetic air exhibit unusual big error bars. The same behaviour can be seen in Rupp et al. [3] (figure 7). Obviously there is some time dependant parameter influencing the samples in the tubular furnace causing increased standard deviations.

In humid atmosphere the amount of water soluble Sr rises much steeper, but not to the same level as in dry atmosphere (only 2.4 times the amount of the as prepared sample). The peak is already reached after 3 h. Afterwards even some decrease of the Sr amount from 2.8 to 2.4 nmol is detectable. Significance can be estimated with a Mann-Whitney-U-Test. The null-hypotheses that the Sr amount of the set of samples at 3 h is equal to the Sr amount at 72 h can be rejected (U_{test} = 0.0 < U_{crit} = 1.0 at 95 %

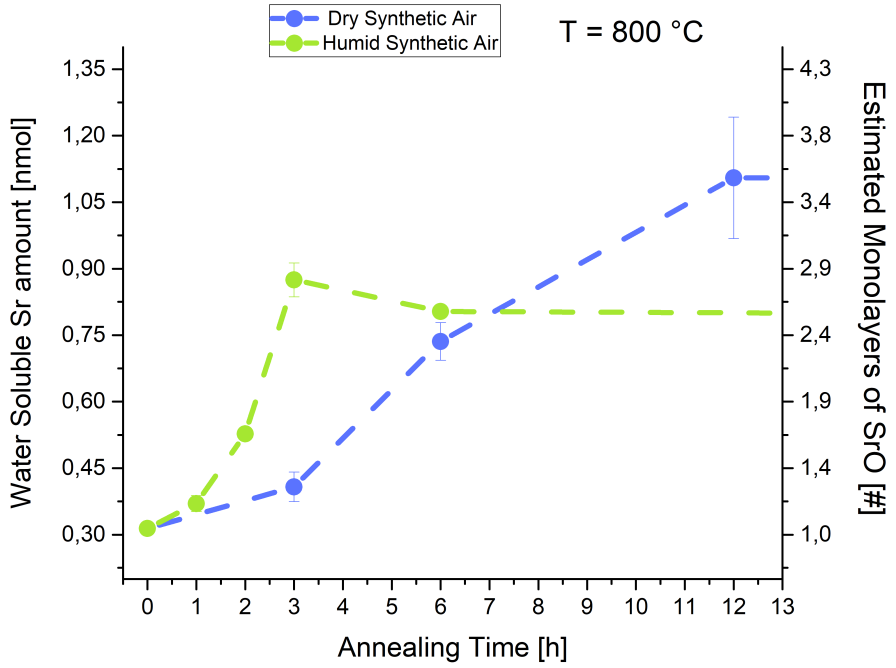

(a) Close-up at short annealing times;

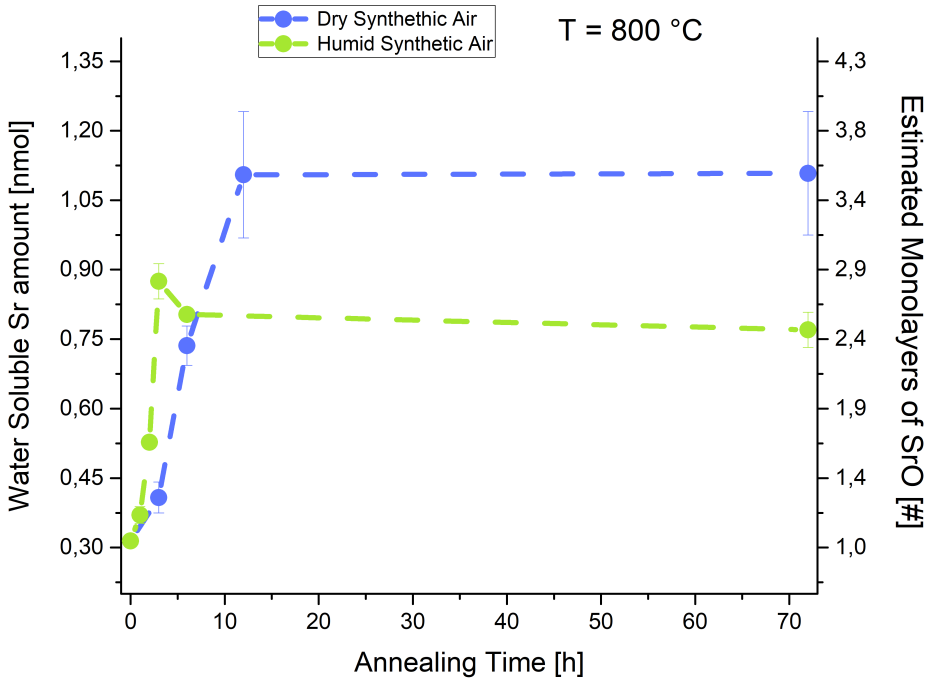

(b) Steady state reached at 72 h annealing time;

FIGURE 4.11: ICP-MS results of H_2O etching after annealing at 800 °C in different atmospheres for different periods of time;

significance). Samples annealed in dry atmosphere show about 40 % more water soluble Sr on the surface than the samples annealed in humid atmosphere after 72 h. In other words, samples annealed with dry synthetic air show 3.5 monolayers of SrO compared to 2.5 monolayers of samples annealed in humid atmosphere.

Obviously the segregation behaviour is different, depending on the presence or absence of H_2O. Different surface morphologies could be one possible explanation. If $Sr(OH)_2$ forms a dense layer on the surface prohibiting Sr cations to diffuse to the surface or H_2O molecules to diffuse into the bulk, the formation of SrO would be stopped at some point. If the SrO film is not dense, but porous or does not produce a diffusion barrier, then it would be possible to form more SrO than $Sr(OH)_2$.

The decrease of water soluble Sr amount with time after 6 h in humid atmosphere may be explained with the chemical stability of bulk $Sr(OH)_2$ which has its melting point at 100 °C and is decomposed at 710 °C. Due to the annealing temperature of 800 °C, it could happen that some amount of $Sr(OH)_2$ is removed by the gas flow. The diffusion of Sr cations from bulk to the surface is getting slower with time, because of the depletion of Sr in the bulk material. Thereof, less $SrO/Sr(OH)_2$ is produced by diffusion of Sr to the surface than removed by the gas stream and so the amount of water soluble Sr detectable with the ICP-MS measurement may be decreased after longer annealing in humid synthetic air.

4.4.2 SEM Images

To get an idea of the morphology of the sample surface and to observe changes during the annealing process, SEM measurements were carried out at the Forschungszentrum Jülich, Germany. In figure 4.12, images of a sample in the as prepared state, after annealing in humid synthetic air and after the H_2O etching procedure are shown. The surface of the as prepared sample in figure 4.12 a) is very homogeneous, flat and crack-free. No crystals protrude from the sample surface. Information about the species of the terminating layer is not given in these pictures. With the knowledge obtained form the ICP-MS measurements in this work and in the LEIS measurements of Rupp et al. [3], $SrO/Sr(OH)_2$ could form this terminating layer. The annealed sample in a humid atmosphere clearly shows precipitates on the surface depicted in figure 4.12 b) and c). These precipitates vanish during the etching process, indicating that these crystals are also made of $SrO/Sr(OH)_2$. After the etching process, the surface appears to be even smoother than in the as prepared state. Assumptions concerning the elemental composition of the surface can not be made, because secondary electron images do not contain such information. Therefore these images solely make changes in the surface topography visible.

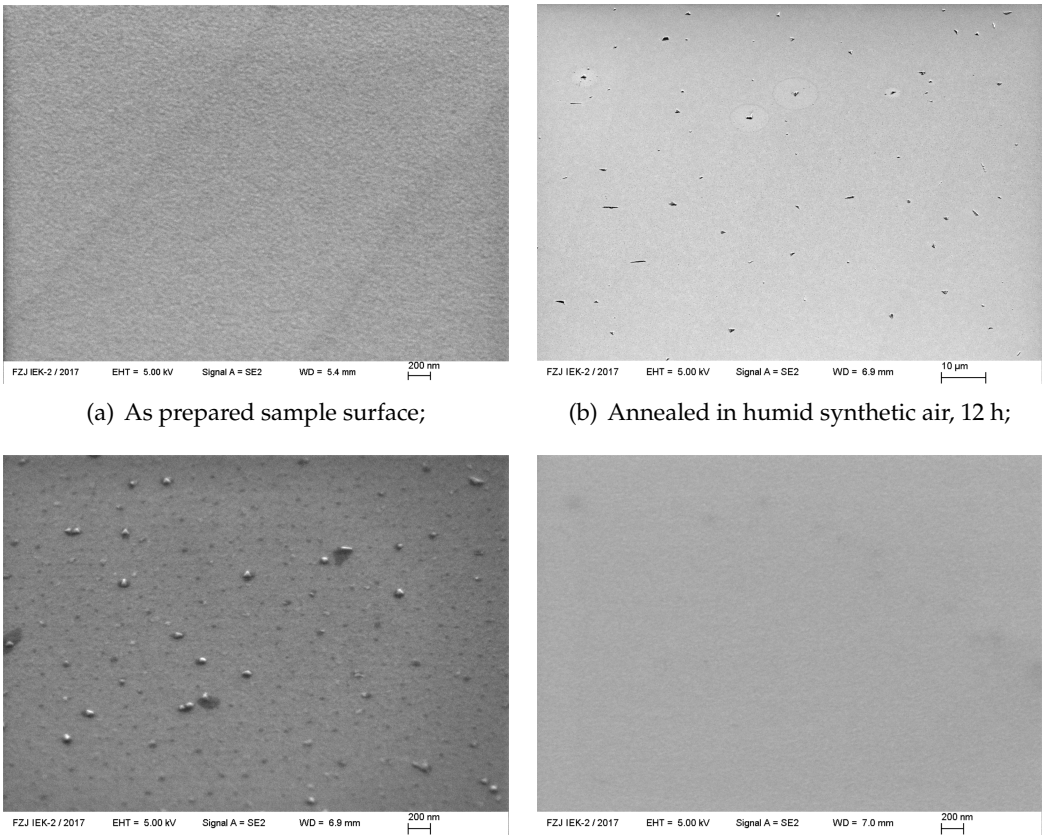

(a) As prepared sample surface;

(b) Annealed in humid synthetic air, 12 h;

(c) Annealed in humid synthetic air, 12 h, close-up;

(d) Surface after H_2O etching procedure;

FIGURE 4.12: SEM images in the secondary electron mode obtained in Forschungszentrum Jülich, Germany;

Chapter 5

Conclusion

Main parts of the presented work focused on the improvement of the quality of thin films produced by PLD. Growing oxide filmy by PLD is a widely spread preparation process in many scientific communities, because it is denoted as a technique capable of producing thin films with defined stoichiometry. In many applications however, slight deviations of the desired stoichiometry may cause dramatic variations of investigated sample characteristics. Therefore analytical methods able to detect such slight deviations in the stoichiometry of these materials are of great interest.

In this work the effect of deposition parameters on the surface and bulk composition of PLD-grown LSCF thin films was studied by means of ICP-MS-based analytical techniques. As reported in literature the surface of as-deposited LSCF films was covered with a SrO layer. However, with the PLD parameters from literature the scattering of ICP-MS data was unsatisfactorily high. Therefore, a systematic variation of deposition parameters was performed.

The variation of the substrate to target distance was the starting point to take a closer look at the PLD process and to find analytical methods to investigate homogeneity of the deposited LSCF films. With liquid ICP-MS measurements, it could be shown that an increase in the substrate to target distance improves the homogeneity of the samples with respect to the water soluble amount of Sr (lowering RSD from 15 to 3 %), but at the costs of stoichiometry loss. Due to the bigger distance, the atoms and ions had to travel, the elemental composition was shifted. The heavier element La could be found more pronounced at the new distance chosen. Thereof, an imbalance between A and B cations of the perovskite was the result.

To shed further light on the inhomogeneities of PLD-grown LSCF films, LA-ICP-MS measurements ware conducted. With this powerful tool it was possible to obtain distribution images of element ratios of a sample with 4.5 cm diameter. Such images can not be found in literature so far. These images give the opportunity to, at least partially, retrace the trajectory of the atoms and ions in the plasma plume. Understanding the dynamics of the plasma plume is crucial for film quality. These elemental distribution images revealed that La preferentially stays in the center of the

plasma plume, whereas lighter elements are pushed further outside. Furthermore, it was observed that two elements with nearly the same atomic mass (Fe and Co) are similarly governed by the driving forces in the plasma plume. This behaviour is interpreted in terms of interaction of ablated atoms or ions in the plasma plume and the gas atmosphere in the PLD chamber. Since trajectories of heavier elements are less influenced by collisions with gas molecules, they keep more concentrated to the center of the plume - for lighter elements the situation is vice versa. This work is another step closer to the recognition that samples produced by a PLD process do not necessarily exhibit the stoichiometry of the target. Indeed there are several parameters influencing the quality and stoichiometry of thin films produced with this method which should be carefully chosen.

After optimization of PLD parameters, in the second part of this work the Sr segregation behaviour at 800 °C in two different atmospheres could be investigated. This temperature was chosen, since it is a typical operation temperature for SOFCs. The obtained data showed substantially different segregation behaviour between samples annealed in dry synthetic air and humidified synthetic air. When using a dry atmosphere about 40 % more water soluble Sr is formed on the LSCF surface compared to samples in a humidified atmosphere, but in contrast, in humid atmosphere the water soluble Sr species is formed four times faster than in the dry atmosphere. It is possible that this behaviour is due to different diffusion characteristics of the Sr rich layers being formed.

Chapter 6

Outlook

The aim of the presented work is not and could not be to examine and explain all the mechanisms and influences of the parameters in the PLD process. This work is a good starting point for further investigations in this field. Actually there are several routes which might be fruitfully rewarded.

On the one hand further parameters of the PLD process could be varied to learn about their influences on the deposited material. Big samples, like the one used for the LA-ICP-MS image could work as screens to reconstruct the trajectories of the elements in the plasma plume. The influence of parameters like laser fluence, pressure of the background gas, pulse rate and substrate temperature has not been systematically investigated yet.

On the other hand with a further development of the analytical method, a lower sensitivity and/or higher accuracy could be gained. There are ideas to replace the He carrier gas in the laser ablation process with a liquid. This liquid should carry the small particles produced by the laser into the MS. This small evolution of the well established LA method could bring tremendous improvements for this technique. For example quantification of samples measured with LA - which is usually a quite expensive task, because of the lack of reference materials - could be done with liquid standard solutions. Although replacing the carrier gas with a liquid sounds fairly easy, many practical problems have to be surmounted.

Furthermore, looking for alternative routes for producing thin films with defined stoichiometry is very interesting, since sample production with the PLD process is very time and energy consuming. Small approaches producing LSCF thin films with a technique called polymer assisted deposition (PAD) could be made during the work for the presented data (progress made in this topic was not shown here). Thereby cations in wanted ratios are dissolved in a polymer solution. This solution can be spin coated onto the surface of YSZ substrates. During the calcination process, the organic phase is removed and the metal oxides are formed. If the parameters were chosen appropriate, a dense and crack free thin film of LSCF is obtained.

List of Figures

List of Tables

Bibliography

[1] S. Bilgen, *Renewable and Sustainable Energy Reviews* **2014**, *38*, 890–902.

[2] A. Franco, A. Russo, *International Journal of Thermal Sciences* **2002**, *41*, 843–859.

[3] G. M. Rupp, H. Tellez, J. Druce, A. Limbeck, T. Ishihara, J. Kilner, J. Fleig, *Journal of Materials Chemistry A* **2015**, *3*, 22759–22769.

[4] N. Mahato, A. Banerjee, A. Gupta, S. Omar, K. Balani, *Progress in Materials Science* **2015**, *72*, 141–337.

[5] S. P. Simner, M. D. Anderson, M. H. Engelhard, J. W. Stevenson, *Electrochemical and Solid-State Letters* **2006**, *9*, A478–A481.

[6] M. Kubicek, A. Limbeck, T. Frömling, H. Hutter, J. Fleig, *Journal of The Electrochemical Society* **2011**, *158*, B727–B734.

[7] Z. Cai, M. Kubicek, J. Fleig, B. Yildiz, *Chemistry of Materials* **2012**, *24*, 1116–1127.

[8] J. Druce, H. Tellez, M. Burriel, M. D. Sharp, L. J. Fawcett, S. N. Cook, D. S. McPhail, T. Ishihara, H. H. Brongersma, J. A. Kilner, *Energy & Environmental Science* **2014**, *7*, 3593–3599.

[9] J. Druce, T. Ishihara, J. Kilner, *Solid State Ionics* **2014**, *262*, 893–896.

[10] H. Wang, K. J. Yakal-Kremski, T. Yeh, G. M. Rupp, A. Limbeck, J. Fleig, S. A. Barnett, *Journal of The Electrochemical Society* **2016**, *163*, F581–F585.

[11] G. M. Rupp, A. K. Opitz, A. Nenning, A. Limbeck, J. Fleig, *Nat Mater* **2017**, *16*, 640–645.

[12] A. Limbeck, G. M. Rupp, M. Kubicek, H. Tellez, J. Druce, T. Ishihara, J. A. Kilner, J. Fleig, *Journal of Analytical Atomic Spectrometry* **2016**, *31*, 1638–1646.

[13] H.-H. Möbius, *Journal of Solid State Electrochemistry* **1997**, *1*, 2–16.

[14] C. Sun, R. Hui, J. Roller, *Journal of Solid State Electrochemistry* **2010**, *14*, 1125–1144.

[15] R. D. Shannon, C. T. Prewitt, *Acta Crystallographica Section B* **1969**, *25*, 925–946.

[16] L. W. Tai, M. M. Nasrallah, H. U. Anderson, D. M. Sparlin, S. R. Sehlin, *Solid State Ionics* **1995**, *76*, 273–283.

[17] A. A. Ammann, *Journal of Mass Spectrometry* **2007**, *42*, 419–427.

[18] S. R. C. Douglas A. Skoog, F. James Holler, Principles of Instrumental Analysis, Sixth Edition, David Harris, **2007**.

[19] D. Beauchemin, *Analytical Chemistry* **2010**, *82*, 4786–4810.

[20] In Inductively Coupled Plasma Mass Spectrometry Handbook, Blackwell Publishing Ltd., **2009**, pp. i–xv.

[21] T. D. Hettipathirana, D. E. Davey, *Journal of Analytical Atomic Spectrometry* **1998**, *13*, 483–488.

[22] N. Yamada, *Spectrochimica Acta Part B: Atomic Spectroscopy* **2015**, *110*, 31–44.

[23] P. R. Willmott, *Progress in Surface Science* **2004**, *76*, 163–217.

[24] Q. Bao, C. Chen, D. Wang, Q. Ji, T. Lei, *Applied Surface Science* **2005**, *252*, 1538–1544.

[25] H. M. Christen, G. Eres, *Journal of Physics: Condensed Matter* **2008**, *20*, 264005.

[26] A. Miotello, R. Kelly, *Applied Physics Letters* **1995**, *67*, 3535–3537.

[27] R. Kelly, A. Miotello, *Physical Review E* **1999**, *60*, 2616–2625.

[28] D. S. Kabekkodu, *ICDD* **2010**, *Set 60*.

[29] G. M. Rupp, A. Limbeck, M. Kubicek, A. Penn, M. Stoger-Pollach, G. Friedbacher, J. Fleig, *Journal of Materials Chemistry A* **2014**, *2*, 7099–7108.

[30] H. Wang, S. A. Barnett, *ECS Transactions* **2017**, *78*, 905–913.

[31] S. Wicklein, A. Sambri, S. Amoruso, X. Wang, R. Bruzzese, A. Koehl, R. Dittmann, *Applied Physics Letters* **2012**, *101*, 131601.

[32] P. Orgiani, R. Ciancio, A. Galdi, S. Amoruso, L. Maritato, *Applied Physics Letters* **2010**, *96*, 032501.

[33] T. Ohnishi, M. Lippmaa, T. Yamamoto, S. Meguro, H. Koinuma, *Applied Physics Letters* **2005**, *87*, 241919.

[34] E. Breckenfeld, R. Wilson, J. Karthik, A. R. Damodaran, D. G. Cahill, L. W. Martin, *Chemistry of Materials* **2012**, *24*, 331–337.

[35] D. Kan, Y. Shimakawa, *Applied Physics Letters* **2011**, *99*, 081907.

[36] J. Schou, *Applied Surface Science* **2009**, *255*, 5191–5198.

[37] A. Ojeda-G-P, C. W. Schneider, M. Döbeli, T. Lippert, A. Wokaun, *Applied Surface Science* **2016**, *389*, 126–134.

[38] R. Sisneros, M. Raji, M. W. Van Moer, D. Bock in Advances in Visual Computing: 12th International Symposium, ISVC 2016, Las Vegas, NV, USA, December 12-14, 2016, Proceedings, Part I, (Eds.: G. Bebis, R. Boyle, B. Parvin, D. Koracin, F. Porikli, S. Skaff, A. Entezari, J. Min, D. Iwai, A. Sadagic, C. Scheidegger, T. Isenberg), Springer International Publishing, Cham, **2016**, pp. 391–402.